

Quantum-corrected NMR crystallography at scale

Matthias Kellner,^{1,+} Ruben Rodriguez-Madrid,^{2,+} Jacob B. Holmes,² Victor Paul Principe,¹
Lyndon Emsley,^{2,*} and Michele Ceriotti^{1,*}

¹ Laboratory of Computational Science and Modeling, Institut des Matériaux, École Polytechnique Fédérale de Lausanne, 1015 Lausanne, Switzerland

² Laboratory of Magnetic Resonance, Institut des Sciences et Ingénierie Chimiques, École Polytechnique Fédérale de Lausanne, 1015 Lausanne, Switzerland

ABSTRACT: Structure determination by chemical-shift-driven NMR crystallography relies on comparing chemical shieldings measured in solid-state NMR experiments with simulations. However, computational cost limits the accuracy of shielding predictions, that usually rely on low-level electronic-structure approximations and neglect thermal and quantum mechanical nuclear motion, leading to large errors, especially for highly informative hydrogen-bonded protons. To address these limitations, we introduce a quantum-nuclei-corrected (QNC-NMR) approach. We generate inexpensively quantum ensembles using PET-MOLS, a novel machine-learning learning model of the interatomic potential transferable across molecular crystals. Using them as inputs to a chemical-shift model results in a two-fold improvement of the agreement with experiments for hydrogen-bonded protons, without the need for empirical corrections. The ability to sample structures consistent with the experimental conditions enables further refinement of the shielding model by finetuning it against measured shieldings. The favorable scaling with system size allows similar improvements for amorphous materials that are otherwise inaccessible to explicit DFT simulations.

INTRODUCTION

Hydrogen bonding is a key structural motif that determines the packing, conformational preferences, and overall three-dimensional structure of soft and condensed organic matter.¹⁻⁴ However, determining the structure of hydrogen bonding motifs with high accuracy is challenging. This is particularly true since hydrogen atoms, with their low electron density, are practically transparent to X-rays.⁵

Solid-state nuclear magnetic resonance (NMR) chemical shifts, in combination with computational methods and diffraction, can be used to routinely elucidate the structure of molecular solids from powder samples.⁶⁻⁹ The pronounced sensitivity of NMR shifts to hydrogen-bonding patterns, together with the applicability of solid-state NMR to amorphous systems, makes it particularly well suited to probe hydrogen-bonded structures in both crystalline and disordered condensed organic matter.¹⁰

Structure determination by chemical-shift driven NMR crystallography relies on comparison of experimentally measured chemical shifts with predictions from complementary *ab initio* calculations that link candidate structural motifs to measured shifts and, in favorable cases, enable full structure determination.^{7-9,11,12} This approach has been successfully applied to resolve the structures of a range of complex materials including cements,^{13,14} photovoltaic perovskites,^{15,16} or powdered and amorphous active pharmaceutical ingredients,

providing a robust basis for the analysis of amorphous drug formulations.¹⁷⁻²²

Paradoxically, chemical shift computations are least reliable for precisely those labile protons and hydrogen-bonding environments where NMR measurements might be most valuable. In the literature, numerous cases have been reported where computed chemical shifts of labile protons significantly deviate from experimental values in both crystalline²³⁻²⁵ and amorphous forms.^{18,20} Such systematic mismatches directly impact the robustness of chemical shift-driven structure determination protocols.

Various factors contribute to this discrepancy. First, experimentally measured chemical shifts are ensemble averages over fast (sub-ns) vibrational and thermal motions, and theoretical predictions must be likewise formulated and computed as averages over ensembles of structures rather than only for the single minimum-energy structures that are typically used due to the computational cost of predicting and sampling the correct thermodynamic ensemble. Notably, the underlying interatomic potential used to generate ensembles of structures must permit bond breakage, which becomes essential in fractional protonation states and hydrogen bond rearrangements. Second, light nuclei – especially protons – are subject to further delocalization due to nuclear quantum effects. Third and finally, any practical approach must be scalable to large

systems containing thousands of atoms to enable the study of realistic complex structures.

Several existing strategies and previous work partially address these limitations. Early works, computing harmonic corrections employing classical forcefields, find significant improvement in the agreement between calculated and predicted values, but cannot correctly describe proton transfer and quantum delocalization.²⁶⁻²⁸ *Ab initio* molecular dynamics, especially in their path integral formulation²⁹ commonly referred as path integral molecular dynamics (PIMD), as performed by Dračinsky, Hodgkinson and Bour in molecular organic solids, showed better agreement of predictions with experimental data.^{30,31} This approach enables rigorous treatment of these effects but prevents studies of larger systems and is typically limited to GGA DFT functionals, which do not reliably yield accurate dissociation energetics.³²

Advances in machine learning (ML) models have removed the computational cost barrier for predicting both shieldings and interatomic forces. Specifically, over the last decade, machine learning interatomic potentials (MLIPs) have emerged as an alternative to overcome the computational expenses of *ab initio* calculations. Those models can rapidly compute energies and atomic forces for both stable and distorted structures, and they can be trained on high-accuracy DFT calculations.³³ Fast and accurate ML models for chemical shielding predictions in molecular solids have also been trained on DFT computed shieldings,³⁴⁻³⁸ due to the lack of large curated databases of experimentally measured chemical shifts. These ML models reduce the computational cost of shift calculations with respect to the equivalent DFT methods by several orders of magnitude while, for the ShiftML3 model, keeping accuracies of 0.53 ppm and 2.44 ppm for ¹H and ¹³C, respectively against experimental benchmark sets.³⁷

Combining both ML shielding models and MLIP for structural sampling allows speeding up chemical shielding computations of static structures and including the effects of finite temperature as well as quantum nuclear delocalization through PIMD simulations. This makes them orders of magnitude faster than *ab initio* quantum calculations and renders them accessible for both longer simulation times and larger systems. Engel *et al.* were the first to report chemical shift computations using jointly bespoke chemical shielding ML models and MLIPs, to describe the effect of finite-temperature and quantum nuclear fluctuations in NMR crystallography for molecular organic solids.³⁹ Similarly, Laurila *et al.* also showed that combining MLIP and ML-shielding models

leads to improved ¹³C chemical shift predictions for the different C₆₀ isomers.⁴⁰ So far, the application of MLIPs to compute NMR observables has been largely limited to specific systems, as traditional MLIPs lack the transferability to general condensed organic matter. More recently, several “universal” MLIPs for either general materials or organic molecules were introduced. These models are commonly trained on large corpora of DFT reference calculations, intended to cover a broad range of compositional space. They yield satisfactory accuracy for general materials modeling problems within their training-domain.⁴¹⁻⁴⁵ The appeal of universal MLIPs lies in their transferability. Like classical all-atoms force fields⁴⁶ universal molecular MLIPs can predict interatomic potentials for almost any organic crystal, without losing much of the *ab initio*-quality bespoke MLIPs promise, nor the ability of treating reactive, bond-breaking events.⁴¹⁻⁴⁵

In this work we introduce an approach that we dub quantum nuclei corrected NMR (QNC-NMR), to include a description of quantum nuclear effects on labile protons and their ¹H chemical shifts in molecular organic solids. Figure 1 illustrates the workflow of the new approach. This is enabled by combining an ML model for chemical shift predictions (ShiftML3) with a newly developed transferable MLIP for molecular organic solids, PET-MOLS, to compute chemical shift averages from PIMD simulations of large-scale systems. We first test the method on a benchmark set of experimentally measured ¹H shifts of organic crystals and on a few challenging case studies for crystalline structures, where we find that the QNC-NMR approach yields a factor two better agreement with experiment for hydrogen-bonded protons. We then apply the new protocol to the prediction of ¹H chemical shifts of labile protons in large scale amorphous structural models of a glucagon-like peptide-1 receptor agonist (GLP-1RA).²⁰

Our analysis relies heavily on the accurate computation of fractional protonation occupancies, which are sensitive to prediction errors of the potential energy, and we demonstrate that the uncertainty estimator of the MLIP is able to identify when the potential energy surface predicts highly uncertain protonation states with respect to the training reference DFT computations.

Finally, we introduce an “ensemble of latent features” (ELF) approach that allows us to reconcile the computational and experimental description of NMR measurements and to build a Δ -ShiftML model that achieves better accuracy by finetuning against experimental references.

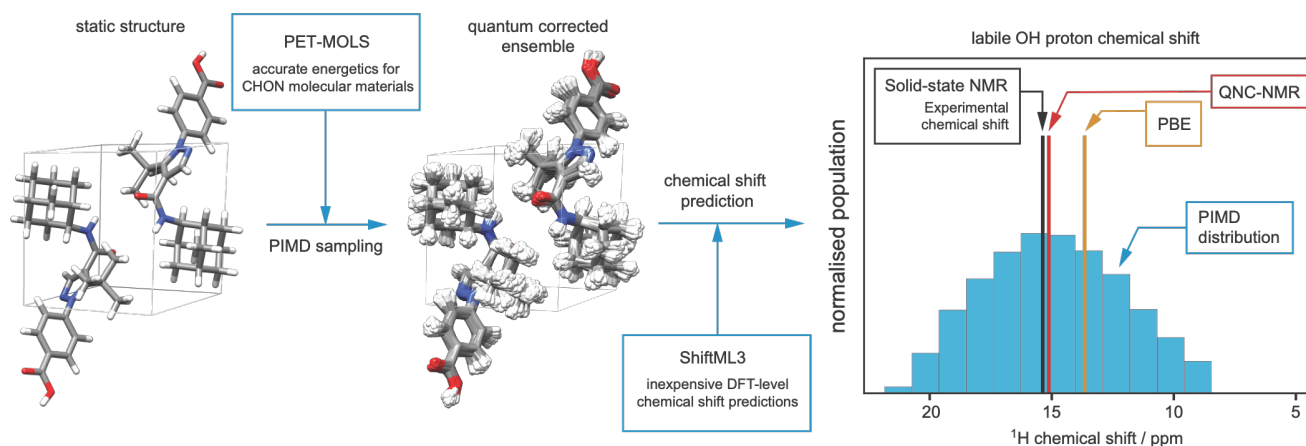


Figure 1. Schematic illustration of the steps for large scale QNC-NMR corrected shift predictions. First, selection of a candidate crystal structure (here Form 4 of AZD8329),⁴⁷ where DFT(PBE) chemical shift predictions for hydrogen-bonded protons (here shown by the orange line in the graph on the right for the OH proton) might typically have errors of ~ 1.5 ppm with respect to the experimentally determined chemical shifts. A PIMD sampling of the static form is run using the MLIP introduced here, dubbed PET-MOLS to generate an ensemble of structures. Chemical shifts are then predicted using the ShiftML3 model, which yields a distribution of chemical shifts (blue histogram). The average of the distribution, dubbed QNC-NMR approach (red line) is now in significantly better agreement with the experimental value.

RESULTS

A transferable potential for organic solids

To be able to efficiently generate ensembles of structures requires an interatomic potential that has the accuracy of DFT and the computational efficiency of an empirical forcefield, and which is transferable across a broad range of organic solids. To this end, we introduce PET-MOLS a ML potential trained on $\sim 10,000$ thermally sampled and relaxed configurations of diverse molecular crystals chosen from the Cambridge structural database (CSD),⁴⁸ that include H, C, N and O atoms.

The structures have been previously sampled to generate the ShiftML2 and ShiftML3 DFT shielding calculation training data.^{48,37} We choose the PBE0+MBD DFT level of theory to generate training data for the ML potential, as PBE0 and hybrid DFT functionals correctly estimate the stability of fractional protonation states^{32,49} and more generally yield unbiased bond length estimates in organic solids over commonly employed GGA functionals.⁵⁰ More details about ML model training and the reference computations are described in the Methods section and in SI. On hold-out test DFT data PET-MOLS achieves a test set accuracy of 3.3 meV/atom for energy and 62.4 meV/Å for forces, and provides excellent accuracy for modeling tasks beyond those we use here. A thorough characterization and validation of the model can be found in the SI.

Chemical shift prediction for crystal structures

Figure 2 shows comparisons between three protocols for predicting (using ShiftML3³⁷) ^1H chemical shifts, benchmarking them on a set of 7 experimentally determined crystalline structures. The first protocol, dubbed Static-PBE, consists of running the predictions on the geometry relaxed structures using density functional theory (DFT) using the PBE density

functional (see Section S1). This approach corresponds to the current standard in the field. The second one, dubbed Static-PBE0, follows the same approach as the first, but uses our new PET-MOLS for the geometry optimization. The last protocol is our QNC-NMR scheme, which consists of computing the averaged chemical shift predictions along a PIMD using PET-MOLS at constant temperature, set to that of the experimentally determined chemical shifts for each structure, and volume; commonly referred as NVT or a canonical ensemble (See detailed information in Methods).

Figure 2 shows that for the Static-PBE-relaxed structures, the overall root mean squared error (RMSE) between chemical shift predictions and experiment for all the ^1H atoms in the set is 0.66 ppm, with a deviation of 1.63 ppm observed specifically for the set of hydrogen-bonded protons with experimentally measured chemical shifts greater than 9.6 ppm.

Using the Static-PBE0-relaxed geometries reduces the overall ^1H error by about 14% (Figure 2b). PET-MOLS was trained on structures calculated at the PBE0 level, and as such these findings are consistent with Ramos *et al.*⁵⁰ who reported a 20–30% improvement in prediction accuracies of carbon and nitrogen GIPAW PBE computed shieldings from PBE0-optimized geometries, which are known to yield more-accurate and unbiased intramolecular bond lengths. In line with this, we also observe an improvement of about 28% for carbon shifts when going from Static-PBE to Static-PBE0 geometries (Figure S1).

Figure 2c shows how a significant further improvement is achieved by incorporating nuclear quantum corrections using the QNC-NMR protocol. Relative to the reference predictions for Static-PBE geometries, this reduces the errors by 25%, (0.66 ppm to 0.50 ppm) for hydrogen and 32% for carbons (2.38 ppm to 1.81 ppm) for all atoms in the experimental benchmarks. As expected, the improvement is particularly

remarkable for the H-bonded sites, for which the prediction error is more than halved (1.63 to 0.75 ppm). On the other

hand, accuracies for non-hydrogen-bonded protons remain the same as for the Static-PBE0 geometries.

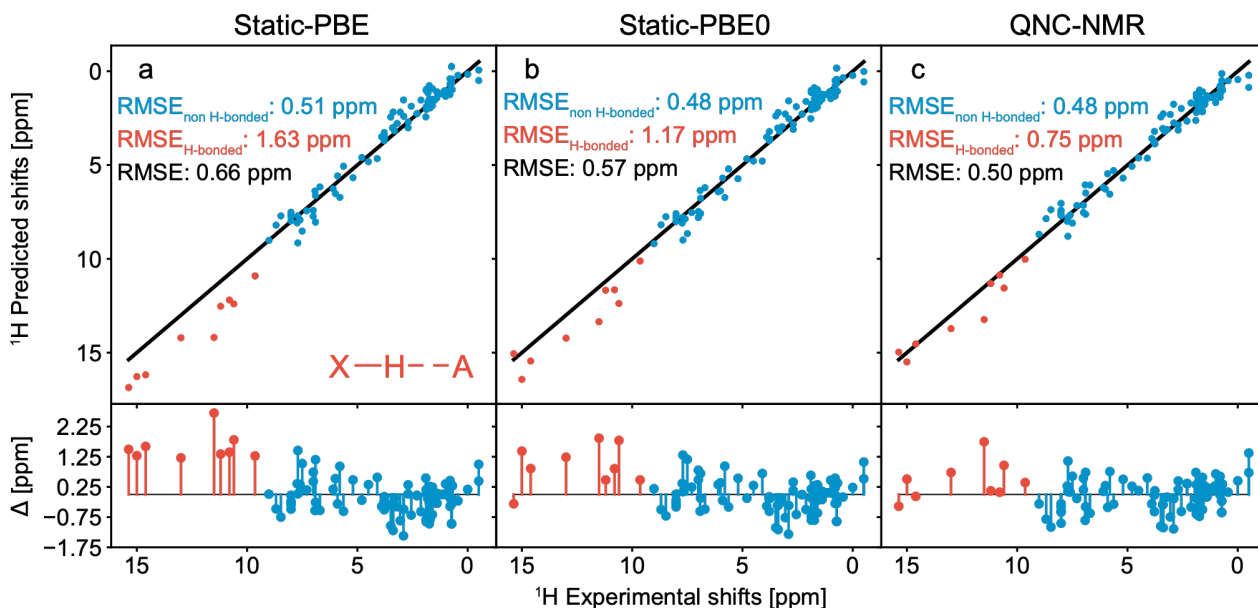


Figure 2. Comparison of experimental and predicted ^1H chemical shifts computed with ShiftML3, using Static-PBE optimized geometries (a), Static-PBE0 optimized geometries (b), and the QNC-NMR approach (c). The black diagonal line in each panel corresponds to a perfect correlation. Red points mark hydrogen-bonded protons in the experimental benchmark set whose experimental chemical shift is greater than 9.6 ppm. The accuracy of the predictions is evaluated with the root-mean square error (RMSE) of all ^1H atoms (in black), the non H-bonded protons ($\text{RMSE}_{\text{non H-bonded}}$, in blue), and the H-bonded protons ($\text{RMSE}_{\text{H-bonded}}$, in red). On the lower panels, Δ is the difference between the predicted and the experimental chemical shift ($\Delta = \delta_{\text{pred}} - \delta_{\text{exp}}$).

Quantifying protonation states

A major advantage of the QNC-NMR protocol over static PBE and PBE0 approaches is its ability to provide an accurate description of fractional protonation states, which are inherently dynamic and cannot be captured within a static electronic-structure framework. Achieving such accuracy critically depends on a faithful representation of the underlying interatomic potential, as subtle changes in hydrogen bonding and proton sharing directly modulate the local magnetic environment. We therefore evaluate the performance of QNC-NMR by comparison with experimental data, focusing on observables that are directly sensitive to proton dynamics. Specifically, we examine the temperature dependence of ^1H chemical shifts, which serve as a direct probe of the evolving hydrogen environment, as well as ^{15}N chemical shifts, which provide an indirect but sensitive measure of the detailed composition of the protonation state.

The temperature-dependent chemical shift of the OH proton in the phenol-pyridine adduct (3-Methyl-4-nitro-phenol / 4-di-methyl-amino-pyridine) is shown in Figure 3a.^{51,52} The shift, previously measured by Štoček *et al.*,⁵² varies monotonically by 1 ppm as the temperature is raised from 173 to 348 K. This was ascribed to a change in protonation state of the intramolecular O-H...N interaction between both components in the cocrystal as the molecule progressively moves from a salt form to a co-crystal as the temperature increases.

Figure 3a shows how the QNC-NMR protocol correctly reproduces the temperature dependence of the protonation state in the structure.

Moreover, ^{15}N chemical shifts are also sensitive probes of protonation states,⁵³ which makes it possible to determine the protonation of an N-H acceptor site, and this has been applied widely.⁵⁴ This high sensitivity makes ^{15}N chemical shift predictions a compelling validation of our framework.

The QNC-NMR protocol also correctly reproduces the ^{15}N chemical shifts for most of the compounds in the benchmark dataset of Ramos *et al.*⁵⁰ (Figure S2). Here two failure cases, GEHHIL (shown in Fig. 3b) and GEHHEH, are worth noting in more detail. The predicted chemical shielding of the nitrogen atom in the Schiff base moieties of GEHHIL and GEHHEH differ by 150 ppm depending on the protonation state of the base motif, as the shared proton exchanges between the base and a neighboring phenolic hydroxyl group. The relative free energy of the two protonation states, that can be inferred straightforwardly from the probability of observing them in simulations, determines the ensemble-averaged chemical shieldings. The built-in uncertainty estimator in PET-MOLS allows us to estimate the uncertainty in the computed free-energy profile as a function of the predicted chemical shift of the Schiff base nitrogen in GEHHIL (Fig. 3c). This reveals that the ML potential, despite its accuracy, cannot

reliably resolve the subtle balance between the two protonation states due to the uncertain estimate of the free energy difference between the protonated and deprotonated base from PET-MOLS. Note that in Fig. 3c we use the chemical shift as the collective variable along which we visualize the free-energy profile, consistent with the general definition of free-energy surfaces in terms of a collective variable that can be any function of the atomic coordinates. Here, choosing the

chemical shift instead of a more traditional geometric collective variable (e.g., the proton-acceptor distance or a proton-transfer coordinate) allows us to directly associate the free-energy uncertainty with a specific chemical-shift range. This example demonstrates the ability of our framework to self-diagnose, and to provide a qualitative aid to the interpretation of experiments, even in cases that are beyond its current energy resolution.

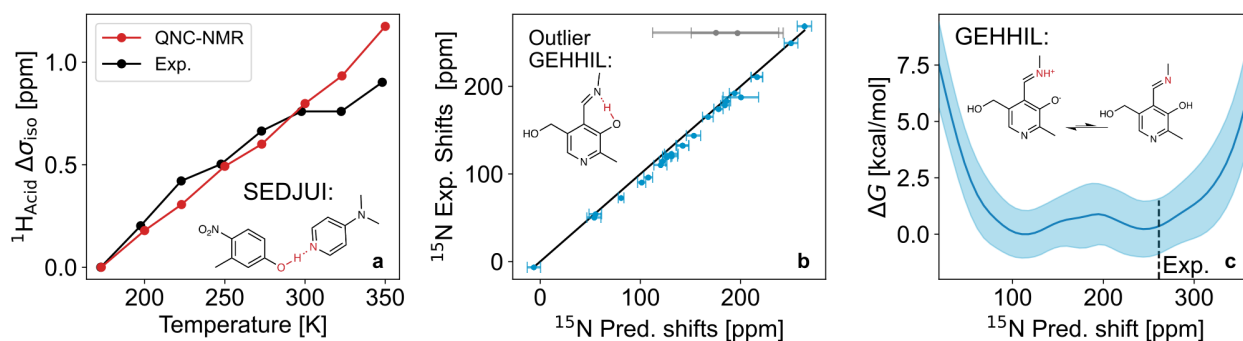


Figure 3. ShiftML3 predictions for the different protonation states. (a) Comparison of the ^1H experimental (data reproduced from ref.⁵²) chemical shifts as a function of temperature with the QNC-NMR predictions in the 3-Methyl-4-nitro-phenol-4-di-methyl-amino-pyridine adduct (with the crystal structure deposited as entry SEDJUI⁵¹ in the CCDC). (b) ^{15}N Chemical shieldings compared to experimental benchmark values computed by ShiftML3 using the QNC-NMR approach. Error bars indicate the uncertainties in potential energy of the PET-MOLS propagated to chemical shieldings. We note the two outliers correspond to the nitrogens in the Schiff Bases of structures GEHHIL (shown inset) and GEHHEH (not shown) where QNC-NMR has high uncertainty of the protonation state (acidic proton highlighted in red). The diagonal black line marks the unit line. (c) Predicted free energy surface of the GEHHIL Schiff base protonation states as a function of the ShiftML3 computed ^{15}N chemical shifts. PET-MOLS propagated uncertainties to the free energy are shown as bands corresponding to one standard deviation of the free energy.

Amorphous structures

We note that studies of small crystalline systems, such as the ones presented in this work, would also be feasible using explicit *ab-initio* calculations, albeit extremely time consuming. They would be however entirely impossible when studying amorphous molecular solids that require models containing thousands of atoms to achieve an accurate description of the distribution of structural features.

As an illustration, we look at the GLP-1RA (**1-Cl**), shown in Figure 4a, constituted of 75 atoms and using structure models for the amorphous solid containing up to 320 molecules. Calculations of the ^1H chemical shifts based on a combination of ShiftML3 and sampling of the amorphous structures using an empirical forcefield (FF-MD) show a large discrepancy for proton shifts of the acidic OH (H42) proton with experiment.²⁰ Specifically, Figure 4b shows the experimental distribution peaks at 13.2 ppm, while the predictions from the structures contained in the FF-MD simulations show a distribution centered at about 8 ppm. To resolve this discrepancy, we apply the PET-MOLS-based sampling protocol using 3 mutated versions of the compound (see SI for the mutation protocol used; mutations were used to substitute the two Cl atoms in the structure, since Cl is outside the current space of PET-MOLS).

Predictions for that labile site using the QNC-NMR protocol for the mutated structure (**1-H**), shown in Figure 4b, now display a marked bimodal separation between hydrogen-bonded and non-hydrogen-bonded environments. For labile protons in hydrogen bonds, the predicted shifts move downfield by about 5 ppm with a mean of 12.6 ppm relative to those obtained from the original FF-MD snapshots.

Figures 4c and 4d show ensemble-averaged predicted chemical shifts using the QNC-NMR protocol as a function of the average proton-transfer coordinate, $v = d(O-H_{42}) - d(H_{42} \cdots A)$ for all the local environments that are hydrogen-bonded for more than 50% of the time over the PIMD sampling using the PET-MOLS. The first observation in Figure 4c is a clear shift of the proton-transfer coordinate in the QNC-NMR approach towards higher values (i.e. stronger H-bonding) compared to the original FF-MD. This is due to the move from a force field based on harmonic potentials towards the incorporation of anharmonic behavior in the inter- and intramolecular interactions from the PET-MOLS trained on electronic calculations. This structural change translates into the dependence of the averaged predicted chemical shift along the trajectories as a function of v , as shown in Figure 4d, where we see a clear increase in the chemical shift. The restriction of the harmonic approximations using the FF based structures limits most of the predicted shifts to around 8 ppm, while the incorporation of finite-temperature and NQE shifts most of

the predictions to around 12.6 ppm, in agreement with Figure 4b.

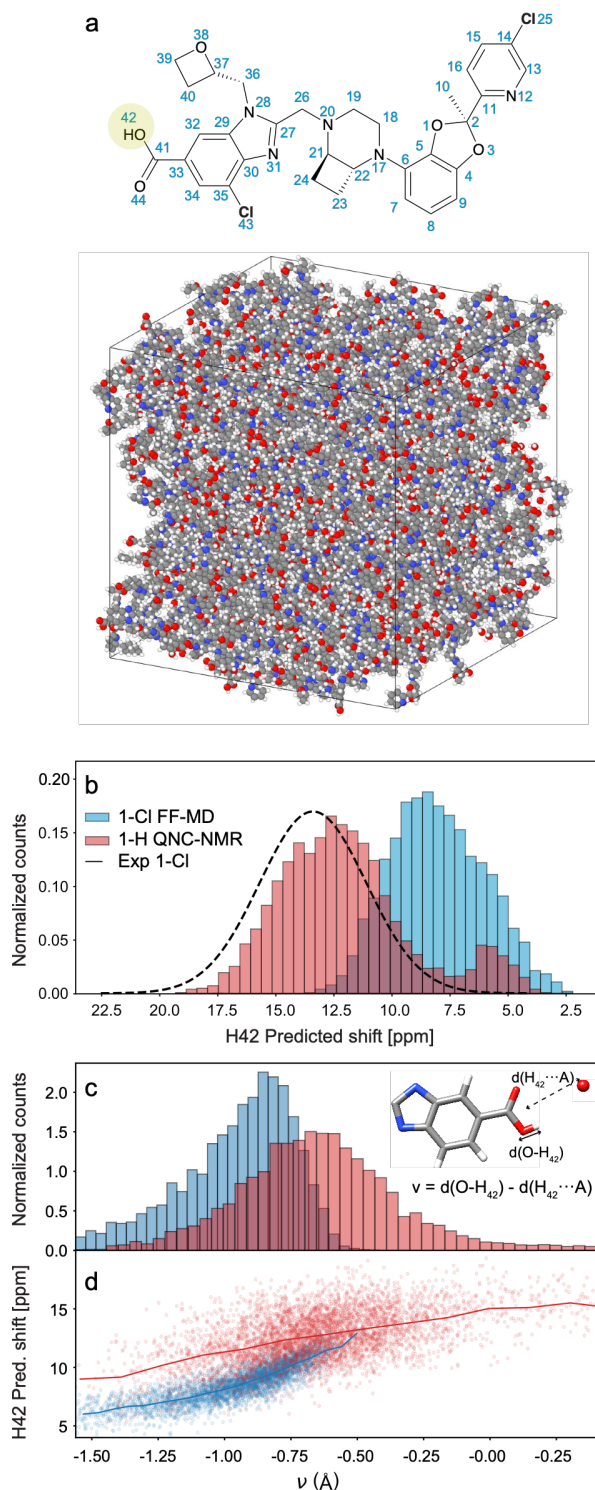


Figure 4. (a) Chemical structure of the GLP-1RA (**1-Cl**) and a snapshot of the amorphous atomistic model employed in this study. (b) Predicted chemical shift distribution for all the molecular environments for **1-Cl** from 17 snapshots selected from the FF-MD trajectories (blue), and the distribution of predicted shifts using the QNC-NMR protocol for each local molecular environment for the **1-H** mutant (red), compared to the experimentally determined chemical shift distribution (dashed black

line) for the labile OH proton (H_{42} in (a)). The experimental distribution is taken from ref²⁰. (c) Normalized distributions as a function of the proton-transfer coordinate, v , for all the hydrogen-bonded atomic OH environments obtained from FF-MD (for **1-Cl**) (blue) and from QNC-NMR (for **1-H**) (red). (d) Predicted 1H chemical shifts as a function of v for the structures in (c). Solid lines represent the mean chemical shift computed within bins of v . In (c) and (d) hydrogen-bonded sites are defined as local atomic environments that participate in a hydrogen bond for more than 50% of the time over the PIMD sampling employing PET-MOLS.

This example provides a striking demonstration of how QNC-NMR crystallography, driven by fast ML surrogate models, provides a qualitatively superior description of H bonding relative to empirical forcefields, and how it can be applied to the size-scales necessary to investigate amorphous solids.

Finetuning from experiment

The ability to sample a representative ensemble of structures consistent with the experimental conditions opens the possibility of refining the shielding model by finetuning it against experiment. To do so requires reconciliation of the ML model for shieldings, that makes predictions for a specific geometry A , and experiment, that measures averages over an ensemble of structures $\{A_i\}$. Using the fact that the last prediction step in our model involves a scalar product between learned features $\Phi(A)$ and a vector of weights w (see SI for details), we can sample thousands of thermalized structures from PIMD simulations at experimental conditions, and from these compute an ensemble of latent features (ELF), $\{\Phi_i = \Phi(A_i)\}$. A corrected weight vector w_{corr} can then be determined by a ridge regression in which the average ELF features are used to predict the experimental shieldings (see Methods). Reducing the complexity of the finetuning problem to a linear model, avoiding overfitting and backpropagating through the entire simulation trajectory when finetuning the ShiftML3 last layer weights, is crucial in light of the limited amount of well curated benchmark experimental data available to us (e.g. 19 compounds for a total of 123 ^{13}C shielding values) and simulation trajectories containing tens of thousands of images. We choose to demonstrate the finetuning via ELF on ^{13}C shielding predictions rather than 1H because, for our purposes, the ^{13}C benchmark set originally proposed by Ramos et al⁵⁰ constitutes to our knowledge the most diverse benchmark set of experimentally measured solid state chemical shifts with unambiguous assignments.

Within the ELF framework we first compute ensemble averages of the ShiftML3 last layer descriptors from PIMD simulations employing PET-MOLS, as well as computing ensemble averages of chemical shieldings using ShiftML3 for the set of 19 reference structures. By minimizing the differences between the computed ensemble and experimental shifts through a Δ model finetuning of the last layer weights of ShiftML3 we obtain an experimentally fine-tuned model of ShiftML3 for the prediction of ^{13}C chemical shieldings. Even with this limited data, the improvement brought by an

experimentally-tuned Δ -ShiftML model is clear, with a reduction of about 0.1 ppm of the RMSE at the largest finetuning set size (Figure 5). Note that, as described in SI, we performed additional tests by either considering fixed or variable regression slopes in preparing the shifts for the Δ -model, as well as removing structure SUCROS04 whose GIPAW/ShiftML computed shifts deviate most from experimental values. Neither change the conclusions of this exercise, demonstrating that the improvement is not due to a few outliers but rather to an overall shift of the error distribution, as shown in the inset of Figure 5.

The Δ -model approach presented here is particularly helpful when learning from data obtained at inconsistent experimental conditions such as varying temperatures, or even mixed liquid and solid-state experiments. The ensemble-average formalism allows to incorporate and mix these conditions during the learning process by simply recreating the experimental conditions in the simulations of the ensemble-average descriptors. Extrapolating from the learning curve shown in Fig. 5, one can estimate that by using shifts from only a few hundred experimental structures would lead to a substantial improvement of the resolving power of NMR crystallography. Generating and making available this data requires a coordinated effort of the solid-state NMR community, and the authors hope that these results may encourage such an endeavor.

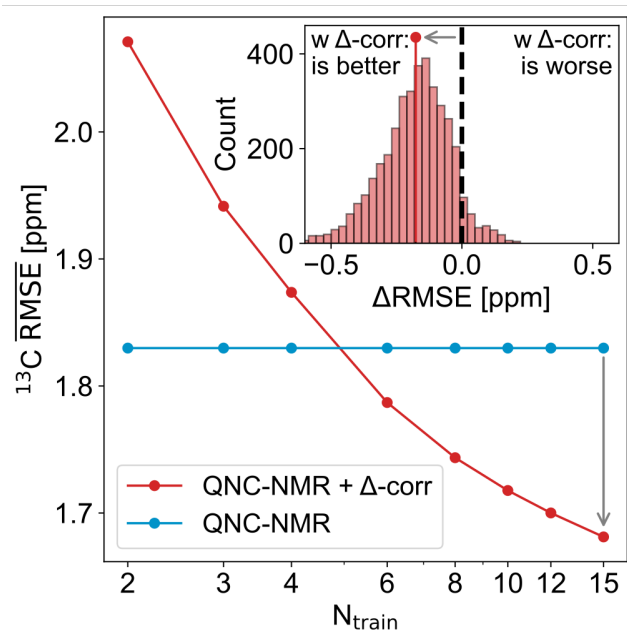


Figure 5. Learning curve of the last layer Δ -correction model for ^{13}C chemical shieldings. The blue curve shows the QNC-NMR ^{13}C reference prediction accuracy, the red curve shows the accuracy of experimentally corrected QNC-NMR predictions. The inset shows a histogram of the improvement in prediction accuracies, ΔRMSE , between uncorrected and corrected predictions considering all $\binom{19}{4}$ splits for the given 19 benchmark structures and fixed test set size of 4 structures. To the left of the dashed line in the inset are training splits for which the test set predictions of the experimentally corrected QNC-NMR shieldings

are more accurate, and to the right are those for which the corrected predictions are less accurate.

DISCUSSION

We have shown how the combination of the generally applicable ML potential PET-MOLS and chemical shielding models enable computational predictions of NMR experiments with unprecedented accuracy and scale. The more accurate electronic-structure reference, as well as the incorporation of finite-temperature and quantum delocalization effects capture the behavior of H-bonded protons without the need for empirical corrections. The result is a factor two reduction (from 1.63 to 0.75 ppm) in the RMSE between ^1H shifts predictions and experiment for H-bonded protons. The availability of inexpensive uncertainty quantification increases further the reliability of the approach revealing the cases in which predictions cannot be trusted. The favorable scaling with system size allows us to show similar improvements for amorphous materials, that are otherwise inaccessible to explicit DFT simulations and constitute one of the most exciting areas of application of NMR crystallography.

The possibility of sampling accurately and at scale the quantum thermodynamic ensemble of molecular materials opens up the opportunity of crossing the boundary between theory and experiments. We demonstrate an ensemble of latent features scheme that can fine-tune a chemical shielding model against the very limited available experimental data, improving the accuracy of NMR structural determination beyond the limits of electronic structure calculations.

REFERENCES

- Pauling, L. *The nature of the chemical bond and the structure of molecules and crystals: An introduction to modern structural chemistry*. 3d edn, (Cornell University Press, 1960).
- Steiner, T. The hydrogen bond in the solid state. *Angewandte Chemie International Edition* **41**, 49-76 (2002).
- Sweetman, A. M., Jarvis, S. P., Sang, H., Lekkas, I., Rahe, P., Wang, Y., Wang, J., Champness, N. R., Kantorovich, L. & Moriarty, P. Mapping the force field of a hydrogen-bonded assembly. *Nature Communications* **5**, 3931 (2014).
- Zhu, K., Reid, O., Rangan, S., Wang, L., Li, J., Antony Jesu Durai, K., Zhou, K., Javed, N., Kasaei, L., Yang, C., Li, M., Sun, Y., Tan, K., Cotlet, M., Liu, Y., Feldman, L. C., O'Carroll, D. M., Zhu, K. & Li, J. Dual interfacial H-bonding-enhanced deep-blue hybrid copper-iodide LEDs. *Nature* **643**, 1246-1254 (2025).
- Egami, T. & Billinge, S. J. L. *Underneath the Bragg Peaks: Structural Analysis of Complex Materials*. Vol. 7 (Elsevier, 2003).
- Bonhomme, C., Gervais, C., Babonneau, F., Coelho, C., Pourpoint, F., Azais, T., Ashbrook, S. E., Griffin, J. M., Yates, J. R., Mauri, F. & Pickard, C. J. First-principles calculation of NMR parameters using the gauge including projector augmented wave method: a chemist's point of view. *Chemical Reviews* **112**, 5733-5779 (2012).
- Ashbrook, S. E. & McKay, D. Combining solid-state NMR spectroscopy with first-principles calculations - a guide to NMR crystallography. *Chemical Communications* **52**, 7186-7204 (2016).

8. Hodgkinson, P. NMR crystallography of molecular organics. *Progress in Nuclear Magnetic Resonance Spectroscopy* **118-119**, 10-53 (2020).
9. Emsley, L. Spiers Memorial Lecture: NMR crystallography. *Faraday Discussions* **255**, 9-45 (2025).
10. Dračinský, M. NMR spectroscopy studies of hydrogen bonding. *Coordination Chemistry Reviews* **549** (2026).
11. Reif, B., Ashbrook, S. E., Emsley, L. & Hong, M. Solid-state NMR spectroscopy. *Nature Reviews Methods Primers* **1** (2021).
12. Bryce, D. L. *Modern NMR Crystallography: Concepts and Applications*. (Royal Society of Chemistry, 2025).
13. Rejmak, P., Dolado, J. S., Stott, M. J. & Ayuela, A. ²⁹Si NMR in Cement: A Theoretical Study on Calcium Silicate Hydrates. *The Journal of Physical Chemistry C* **116**, 9755-9761 (2012).
14. Kumar, A., Walder, B. J., Kunhi Mohamed, A., Hofstetter, A., Srinivasan, B., Rossini, A. J., Scrivener, K., Emsley, L. & Bowen, P. The Atomic-Level Structure of Cementitious Calcium Silicate Hydrate. *The Journal of Physical Chemistry C* **121**, 17188-17196 (2017).
15. Hope, M. A., Nakamura, T., Ahlawat, P., Mishra, A., Cordova, M., Jahanbakhshi, F., Mladenovic, M., Runjhun, R., Merten, L., Hinderhofer, A., Carlsen, B. I., Kubicki, D. J., Gershoni-Poranne, R., Schneeberger, T., Carbone, L. C., Liu, Y., Zakeeruddin, S. M., Lewinski, J., Hagfeldt, A., Schreiber, F., Rothlisberger, U., Gratzel, M., Milic, J. V. & Emsley, L. Nanoscale Phase Segregation in Supramolecular pi-Templating for Hybrid Perovskite Photovoltaics from NMR Crystallography. *Journal of the American Chemical Society* **143**, 1529-1538 (2021).
16. Brivio, F., Sarsembek, N., Martelli, G., Scotillo, R., Loprete, F., De Angelis, F. & Cortecchia, D. Discerning two-dimensional metal halide perovskite moieties using solid-state NMR fingerprints. *J Mater Chem A* **13**, 33739-33748 (2025).
17. Cordova, M., Balodis, M., Hofstetter, A., Paruzzo, F., Nilsson Lill, S. O., Eriksson, E. S. E., Berruyer, P., Simoes de Almeida, B., Quayle, M. J., Norberg, S. T., Svensk Ankarberg, A., Schantz, S. & Emsley, L. Structure determination of an amorphous drug through large-scale NMR predictions. *Nature Communications* **12**, 2964 (2021).
18. Cordova, M., Moutzouri, P., Nilsson Lill, S. O., Cousen, A., Kearns, M., Norberg, S. T., Svensk Ankarberg, A., McCabe, J., Pinon, A. C., Schantz, S. & Emsley, L. Atomic-level structure determination of amorphous molecular solids by NMR. *Nature Communications* **14**, 5138 (2023).
19. Holmes, J. B., Torodii, D., Balodis, M., Cordova, M., Hofstetter, A., Paruzzo, F., Nilsson Lill, S. O., Eriksson, E., Berruyer, P., Simoes de Almeida, B., Quayle, M., Norberg, S., Ankarberg, A. S., Schantz, S. & Emsley, L. Atomic-level structure of the amorphous drug atuliflapon via NMR crystallography. *Faraday Discussions* **255**, 342-354 (2025).
20. Torodii, D., Cordova, M., Holmes, J. B., Moutzouri, P., Casalini, T., Nilsson Lill, S. O., Pinon, A. C., Knee, C. S., Svensk Ankarberg, A., Putra, O. D., Schantz, S. & Emsley, L. Three-Dimensional Atomic-Level Structure of an Amorphous Glucagon-Like Peptide-1 Receptor Agonist. *Journal of the American Chemical Society* **147**, 17077-17087 (2025).
21. Torodii, D., Holmes, J. B., Cordova, M., Moutzouri, P., van Beek, L., Edfeldt, F., Malmerberg, E., Friis, S. D., Johansson, J. R., Milbradt, A. G., Nilsson Lill, S. O., Malfait, B., Schantz, S. & Emsley, L. Determination of key functional structures of an amorphous VHL-based SMARCA2 PROTAC. *Nature Communications* **16**, 9694 (2025).
22. Guest, J. L., Bourne, E. A. E., Screen, M. A., Wilson, M. R., Pham, T. N. & Hodgkinson, P. The essential synergy of MD simulation and NMR in understanding amorphous drug forms. *Faraday Discussions* **255**, 325-341 (2025).
23. Baias, M., Widdifield, C. M., Dumez, J. N., Thompson, H. P., Cooper, T. G., Salager, E., Bassil, S., Stein, R. S., Lesage, A., Day, G. M. & Emsley, L. Powder crystallography of pharmaceutical materials by combined crystal structure prediction and solid-state ¹H NMR spectroscopy. *Physical Chemistry Chemical Physics* **15**, 8069-8080 (2013).
24. Dračinský, M., Vicha, J., Bártoová, K. & Hodgkinson, P. Towards Accurate Predictions of Proton NMR Spectroscopic Parameters in Molecular Solids. *Chemphyschem* **21**, 2075-2083 (2020).
25. Corlett, E. K., Blade, H., Hughes, L. P., Sidebottom, P. J., Walker, D., Walton, R. I. & Brown, S. P. Investigating discrepancies between experimental solid-state NMR and GIPAW calculation: N=C-N ¹³C and OH•••O ¹H chemical shifts in pyridinium fumarates and their cocrystals. *Solid State Nucl Mag* **108** (2020).
26. Dumez, J. N. & Pickard, C. J. Calculation of NMR chemical shifts in organic solids: Accounting for motional effects. *Journal of Chemical Physics* **130**, 104701 (2009).
27. De Gortari, I., Portella, G., Salvatella, X., Bajaj, V. S., van der Wel, P. C. A., Yates, J. R., Segall, M. D., Pickard, C. J., Payne, M. C. & Vendruscolo, M. Time Averaging of NMR Chemical Shifts in the MLF Peptide in the Solid State. *Journal of the American Chemical Society* **132**, 5993-6000 (2010).
28. Dračinský, M. & Hodgkinson, P. A molecular dynamics study of the effects of fast molecular motions on solid-state NMR parameters. *CrystEngComm* **15** (2013).
29. Markland, T. E. & Ceriotti, M. Nuclear quantum effects enter the mainstream. *Nature Reviews Chemistry* **2** (2018).
30. Dračinský, M. & Hodgkinson, P. Effects of quantum nuclear delocalisation on NMR parameters from path integral molecular dynamics. *Chemistry-A European Journal* **20**, 2201-2207 (2014).
31. Dračinský, M., Bour, P. & Hodgkinson, P. Temperature Dependence of NMR Parameters Calculated from Path Integral Molecular Dynamics Simulations. *Journal of Chemical Theory and Computation* **12**, 968-973 (2016).
32. Bal, K. M. & Collas, A. Charting the salt-cocrystal continuum of acid-base multicomponent crystals with hybrid density functional theory. *CrystEngComm* **26**, 6765-6773 (2024).
33. Behler, J. & Parrinello, M. Generalized neural-network representation of high-dimensional potential-energy surfaces. *Physical Review Letters* **98** (2007).
34. Paruzzo, F. M., Hofstetter, A., Musil, F., De, S., Ceriotti, M. & Emsley, L. Chemical shifts in molecular solids by machine learning. *Nature Communications* **9**, 4501 (2018).
35. Cordova, M., Engel, E. A., Stefaniuk, A., Paruzzo, F., Hofstetter, A., Ceriotti, M. & Emsley, L. A Machine Learning Model of Chemical Shifts for Chemically and Structurally Diverse Molecular Solids. *The Journal of Physical Chemistry C* **126**, 16710-16720 (2022).
36. Li, J., Liang, J., Wang, Z., Ptaszek, A. L., Liu, X., Ganoe, B., Head-Gordon, M. & Head-Gordon, T. Highly Accurate Prediction of NMR Chemical Shifts from Low-Level Quantum Mechanics Calculations Using Machine Learning. *Journal of Chemical Theory and Computation* **20**, 2152-2166 (2024).
37. Kellner, M., Holmes, J. B., Rodriguez-Madrid, R., Viscosi, F., Zhang, Y., Emsley, L. & Ceriotti, M. A deep learning model for chemical shieldings in molecular organic solids including anisotropy. *The Journal of Physical Chemistry Letters* **16**, 8714-8722 (2025).
38. Ben Mahmoud, C., Rosset, L. A. M., Yates, J. R. & Deringer, V. L. Graph-neural-network predictions of solid-state NMR parameters in silica from spherical tensor decomposition. *Journal of Chemical Physics* **163** (2025).
39. Engel, E. A., Kapil, V. & Ceriotti, M. Importance of Nuclear Quantum Effects for NMR Crystallography. *The Journal of Physical Chemistry Letters* **12**, 7701-7707 (2021).

40. Laurila, O., Jacklin, T., Zakary, O. & Lantto, P. Machine Learning-Accelerated Path Integral Molecular Dynamics and ^{13}C NMR Simulations Unlock New Insights Into Quantum Effects in C_{60} Fullerene. Preprint at <https://doi.org/10.26434/chemrxiv-2025-68g6s-v> (2025)
41. Smith, J. S., Isayev, O. & Roitberg, A. E. ANI-1: an extensible neural network potential with DFT accuracy at force field computational cost. *Chemical Science* **8**, 3192-3203 (2017).
42. Kovács, D. P., Moore, J. H., Browning, N. J., Batatia, I., Horton, J. T., Pu, Y. X., Kapil, V., Witt, W. C., Magdau, I. B., Cole, D. J. & Csányi, G. MACE-OFF: Short-Range Transferable Machine Learning Force Fields for Organic Molecules. *Journal of the American Chemical Society* **147**, 17598-17611 (2025).
43. Kabylda, A., Frank, J. T., Suarez-Dou, S., Khabibrakhmanov, A., Medrano Sandonas, L., Unke, O. T., Chmiela, S., Muller, K. R. & Tkatchenko, A. Molecular Simulations with a Pretrained Neural Network and Universal Pairwise Force Fields. *Journal of the American Chemical Society* **147**, 33723-33734 (2025).
44. Plé, T., Adjoua, O., Benali, A., Posenitskiy, E., Villot, C., Lagardère, L. & Piquemal, J.-P. A Foundation Model for Accurate Atomistic Simulations in Drug Design. Preprint at <https://doi.org/10.26434/chemrxiv-2025-flhgn-v4> (2025)
45. Anstine, D. M., Zubatyuk, R. & Isayev, O. AIMNet2: a neural network potential to meet your neutral, charged, organic, and elemental-organic needs. *Chemical Science* **16** (2025).
46. Jorgensen, W. L., Maxwell, D. S. & Tirado-Rives, J. Development and Testing of the OPLS All-Atom Force Field on Conformational Energetics and Properties of Organic Liquids. *Journal of the American Chemical Society* **118**, 11225-112236 (1996).
47. Baias, M., Dumez, J. N., Svensson, P. H., Schantz, S., Day, G. M. & Emsley, L. De novo determination of the crystal structure of a large drug molecule by crystal structure prediction-based powder NMR crystallography. *Journal of the American Chemical Society* **135**, 17501-17507 (2013).
48. Groom, C. R., Bruno, I. J., Lightfoot, M. P. & Ward, S. C. The Cambridge Structural Database. *Acta Crystallographica Section B: Structural Science, Crystal Engineering and Materials* **72**, 171-179 (2016).
49. Chalupná, S., Husák, M., Cejka, J., Fňukal, F. & Klimes, J. Computation screening for incorrectly determined cocrystal structures. *Acta Crystallographica Section B: Structural Science, Crystal Engineering and Materials* **81**, 208-216 (2025).
50. Ramos, S. A., Mueller, L. J. & Beran, G. J. O. The interplay of density functional selection and crystal structure for accurate NMR chemical shift predictions. *Faraday Discuss* **255**, 119-142 (2025).
51. Muralidharan, S., Nagapandiselvi, P., Srinivasan, T., Gopalakrishnan, R. & Velmurugan, D. 3-Methyl-4-nitrophenol-4-dimethyl-amino-pyridine (1/1). *Acta Crystallographica Section E: Structure Reports Online* **68**, o3106 (2012).
52. Stoeck, J. R., Socha, O., Cisarova, I., Slanina, T. & Dracinsky, M. Importance of Nuclear Quantum Effects for Molecular Cocrystals with Short Hydrogen Bonds. *Journal of the American Chemical Society* **144**, 7111-7116 (2022).
53. Marek, R., Lycka, A., Kolehmainen, E., Sievänen, E. & Tousek, J. ^{15}N NMR Spectroscopy in Structural Analysis: An Update (2001-2005). *Curr Org Chem* **11**, 1154-1205 (2007).
54. Kalakewich, K., Iulicci, R., Mueller, K. T., Eloranta, H. & Harper, J. K. Monitoring the refinement of crystal structures with N solid-state NMR shift tensor data. *Journal of Chemical Physics* **143** (2015).
55. Pozdnyakov, S. N. & Ceriotti, M. in *Advances in Neural Information Processing Systems* 79469-79501 (2023).
56. Imbalzano, G., Anelli, A., Giofre, D., Klees, S., Behler, J. & Ceriotti, M. Automatic selection of atomic fingerprints and reference configurations for machine-learning potentials. *The Journal of Chemical Physics* **148**, 241730 (2018).
57. Perdew, J. P., Ernzerhof, M. & Burke, K. Rationale for mixing exact exchange with density functional approximations. *The Journal of Chemical Physics* **105**, 9982-9985 (1996).
58. Ambrosetti, A., Reilly, A. M., DiStasio, R. A., Jr. & Tkatchenko, A. Long-range correlation energy calculated from coupled atomic response functions. *The Journal of Chemical Physics* **140**, 18A508 (2014).
59. Litman, Y., Kapil, V., Feldman, Y. M. Y., Tisi, D., Begusic, T., Fidanyan, K., Fraux, G., Higer, J., Kellner, M., Li, T. E., Pos, E. S., Stocco, E., Trenins, G., Hirshberg, B., Rossi, M. & Ceriotti, M. i-PI 3.0: A flexible and efficient framework for advanced atomistic simulations. *The Journal of Chemical Physics* **161** (2024).
60. Ceriotti, M., Parrinello, M., Markland, T. E. & Manolopoulos, D. E. Efficient stochastic thermostating of path integral molecular dynamics. *The Journal of Chemical Physics* **133**, 124104 (2010).
61. Bigi, F., Abbott, J. W., Loche, P., Mazitov, A., Tisi, D., Langer, M. F., Goscinski, A., Pegolo, P., Chong, S., Goswami, R., Chorna, S., Kellner, M., Ceriotti, M. & Fraux, G. Metatensor and metatomic: foundational libraries for interoperable atomistic machine learning. Preprint at <https://arxiv.org/abs/2508.15704> (2025)
62. Ceriotti, M. & Manolopoulos, D. E. Efficient First-Principles Calculation of the Quantum Kinetic Energy and Momentum Distribution of Nuclei. *Physical Review Letters* **109** (2012).
63. Kellner, M. & Ceriotti, M. Uncertainty quantification by direct propagation of shallow ensembles. *Machine Learning: Science and Technology* **5** (2024).
64. Bigi, F., Chong, S., Ceriotti, M. & Grasselli, F. A prediction rigidity formalism for low-cost uncertainties in trained neural networks. *Machine Learning: Science and Technology* **5** (2024).
65. Imbalzano, G., Zhuang, Y. B., Kapil, V., Rossi, K., Engel, E. A., Grasselli, F. & Ceriotti, M. Uncertainty estimation for molecular dynamics and sampling. *The Journal of Chemical Physics* **154** (2021).

METHODS

Machine learning interatomic potential

We construct a machine learning potential for organic crystals at the PBE0+MBD DFT level of theory based on the point-edge transformer architecture (PET) from Pozdnyakov and Ceriotti.⁵⁵ This ML potential is referred to as PET-MOLS in this work. The training data was selected via farthest point sampling (FPS)⁵⁶ from the Cambridge Structural Database (CSD)⁴⁸ to cover a broad range of structural motifs, with the aim of making the potential broadly applicable and transferrable across molecular solids. The pool of candidates of the CSD database was limited to structures containing at most the elements H, C, N, O and up to 200 atoms to restrict memory and computational costs of reference computation. Experimental crystal structures were geometry relaxed using PBE-D2 and for each unique composition four thermally distorted structures were generated from short molecular dynamics simulations at 300 K using PBE-D2. The final training dataset consisted of 2,013 unique organic crystal compositions with a total of 10,056 training structures computed at the PBE0 level of

theory⁵⁷ with many-body dispersion (MBD).⁵⁸ Further information about reference DFT calculation, and the machine learning training of the model are reported in Section S3 in the SI. All computational experiments were performed without further finetuning of the PET-MOLS, underlining the transferability of the proposed MLIP across the space of organic solids.

Reference computations

Reference PBE0+MBD calculations were performed with FHI-AIMS (version 210716.2) using "intermediate" 2020 default basis set definitions and a k-point density of 0.05 Å⁻¹. Dispersion corrections were computed using non self-consistent MBD@rsSCS corrections in their original formulation. Reference FHI-AIMS input and output files are made available in the Materials Cloud archive, associated with this publication.

Experimental benchmark of crystalline structures and NMR predicted chemical shifts

We first evaluate the accuracy of ¹H chemical shift predictions from static and QNC-NMR computations against a set of experimental benchmark structures from previous ShiftML publications.^{34,35} The same evaluation was done for ¹³C and ¹⁵N experimental benchmarks from Ramos et al.⁵⁰ Only structures containing H, C, O, and N were included, consistent with the elemental coverage of the PET-MOLS training set.

In this study, we use the ShiftML3 machine learning model to predict chemical shieldings.³⁷ Shieldings σ are commonly converted to chemical shifts δ using a linear relation, $\delta = a\sigma + b$; and the prediction accuracy is evaluated via the root-mean-square error (RMSE) with respect to the experimental benchmark. In the best case, the fitting equation yields a slope of $a = -1$ indicating, that there is no systematic error, and this is the approach considered in this work for both crystalline and amorphous solids. Nonetheless, in literature fitting the slope has been shown to partially cancel out systematic errors, hence further discussion about fitted slope on the crystalline experimental benchmarks is discussed in Section S1 in the SI.

Amorphous structures

The amorphous structure of the glucagon-like peptide-1 receptor agonist (GLP-1RA, **1-Cl**) recently published in our group²⁰ marks an interesting case for our approach as the labile proton site exhibit large deviations between predicted and experimental shifts distributions. This is not an isolated case as a systematic offset has also been observed on those local environments¹⁸ responsible of the amorphous stabilization.¹⁷⁻¹⁹

We focus on correcting labile proton chemical shift predictions via the QNC-NMR protocol in amorphous structures of a series of chemically mutated derivatives of a GLP-1RA (**1-Cl**) agonist. The reasons of that choice are that the training set for PET-MOLS does not contain Cl atoms, and that only about 1% of those sites were acting as acceptors in the hydrogen-bond network responsible of the amorphous stabilization. Specifically, we consider analogues in which the chlorine substituent is replaced by hydrogen (**1-H**), a methyl group (**1-**

Me), or a nitrile (**1-CN**). In Section S2 we study the acceptors counts for the different mutants showing negligible effects of the mutations on the hydrogen bond network after geometry optimization using PET-MOLS.

In this work, 17 MD random snapshots among all the reference MD generated ones in the original work²⁰ are selected as a test case.

Reference molecular dynamics – amorphous structures

1-Cl and solvent molecules were optimized at the B3LYP-D3/6-31G** level, and CHELPG partial charges were derived from the corresponding electrostatic potentials. The **1-Cl**, n-heptane and 2-MeTHF were parametrized using OPLS-2005, while water was modeled with TIP3P. Three systems were constructed – pure amorphous, C1c and C2b – using the Amorphous Cell module in Materials Studio. The composition of the solvent in the last two systems mention was varied while keeping the composition of the system the closest to experimental. Nonetheless, all systems contain 320 **1-Cl** structures. Then, five amorphous cubic cells were generated per system using COMPASS-II to provide consistent starting configurations.

GROMACS 2016.4 was used to run molecular simulations on all five independent replicas per system. Each trajectory underwent energy minimization, followed by a 1 ns NVT equilibration at 298 K using a Berendsen thermostat ($\tau = 0.1$ ps). Production runs consisted of 1 μ s NPT simulations at 298 K and 1 atm using the stochastic velocity-rescale thermostat ($\tau = 0.1$ ps) and the Parrinello–Rahman barostat ($\tau = 4$ ps). PME was applied for electrostatics with a 1 nm cutoff, also used for van der Waals interactions; long-range dispersion corrections were included. All bonds involving hydrogen were constrained with LINCS, enabling a 2 fs timestep. Periodic boundary conditions were applied in all directions, and configurations were saved every 10 ps.

Only the last 200 ns of each replica were used for postprocessing; equilibration was assessed by monitoring the potential energy and the density as a function of simulation time. One snapshot every 100 ps was extracted from molecular trajectories, corresponding to 2000 snapshots per replica and 10,000 snapshots in total for each system.

Path integral molecular dynamics

Path-integral molecular dynamics (PIMD) simulations were performed with i-PI (version 3.1)⁵⁹ using 32 beads in the NVT ensemble at the respective experimental temperatures. For the organic crystal benchmark set, simulations were run for 50 ps with a timestep of 0.5 fs, and a local PILE-L thermostat⁶⁰ with a damping time of 100 fs used for thermostating the centroid and a coupling parameter $\lambda = 0.1$ for the other normal modes, using 32 beads in the NVT ensemble at the respective experimental temperatures.

For the amorphous systems, snapshots from classical force-field (FF-MD) trajectories were first relaxed using the PET-MOLS via the metatomic LAMMPS interface,⁶¹ followed by a pre-equilibration for ~200 ps running a classical NVT MD at 300 K using PET-MOLS and finally a 2ps PIGLET-accelerated-PIMD simulation using 8-beads.⁶² In Section S2 it is shown the effect on structural changes in the hydrogen bond network for the Static-PBE0 geometries and the evolution of the averaged acidic H42 predicted shift along the simulations. All PIMD simulations of the experimental benchmark set were run at the respective experimental temperature. For the averaged chemical shift only the last ps of the PIMD was considered.

Uncertainty quantification of thermodynamic averages

The PET-MOLS is equipped with a last layer ensemble uncertainty estimator, predicting efficiently a committee of energies for each structure.^{63,64} The spread, or standard deviation of this committee of energy prediction serves as an estimate for the uncertainty of the predicted potential energy. The committee uncertainty estimates can then be propagated to a derived quantity, such as PIMD averages of chemical shifts, via thermodynamic reweighting, which avoids having to run multiple molecular dynamics simulations. Instead, a post-processing step generates a committee of reweighted thermodynamic averages from a single MD trajectory. In practice a statistically more stable, cumulants based expansion is chosen for reweighting:⁶⁵

$$\langle y \rangle_{V^{(k)}} \approx \langle y \rangle_{\bar{V}} - \beta [\langle y(V^{(k)} - \bar{V}) \rangle_{\bar{V}} - \langle y \rangle_{\bar{V}} \langle V^{(k)} - \bar{V} \rangle_{\bar{V}}] \quad (1)$$

Here, $\langle y \rangle_{\bar{V}}$ is the canonical ensemble average of an observable y taken under the committee mean potential (sampling using PET-MOLS), β is the thermodynamic beta, $V^{(k)}$ is the potential energy prediction of the committee member k , \bar{V} is the mean potential energy prediction of the committee and $\langle y \rangle_{V^{(k)}}$ is approximately the canonical ensemble average for a given configuration, obtained after applying (1) instead of explicit molecular dynamics sampling using $V^{(k)}$.

The free energy surface (FES) is the logarithm of a partially integrated partition function, obtained by marginalizing over all microscopic degrees of freedom q . In practices, this reduces the number of remaining degrees of freedom according to arbitrarily defined collective variables with lower dimensionality, that maps a configuration q to a selected number of variables $z = \chi(q)$. This variable can also be the ShiftML3 predicted chemical shielding, and the resulting chemical shielding FES can therefore be expressed as the negative logarithm of $p(\sigma_{\text{iso}})$ the probability of finding a configuration at a given shielding value:

$$F(\sigma_{\text{iso}}) = -k_B T \ln(p(\sigma_{\text{iso}})) \quad (2)$$

In practice $p(\sigma_{\text{iso}})$ can be computed from MD and PIMD simulations via histograms or kernel-density estimates (KDE).

Learning from experiments

We adopt a last-layer finetuning, writing ShiftML3 predictions as $\omega^\top \Phi(A_i)$ a product between a linear set of weights ω and a feature map $\Phi(A_i)$ that transforms the local atomic environment A_i into a fixed-size descriptor. Adapting this linearization, ensemble-averaged ShiftML predictions are straightforward to compute, and determining the corrected weights ω_{corr} that minimizes expression (3) reduces to a linear regression problem:

$$\Delta\sigma = (\sigma_{\text{iso,exp.}} - \omega_{\text{corr}}^\top \langle \Phi(A_i) \rangle)^2 \quad (3)$$

Due to the rather small number of training samples, and its conceptual simplicity, we minimize (3) using a delta model that corrects QNC-NMR predictions. The final corrected predictions are then obtained as $\sigma_{\text{corr}} = \sigma_{\text{QNC-NMR}} + \omega_{\text{corr}}^\top \langle \Phi(A_i)_{\text{SML3}} \rangle$, where $\langle \Phi(A_i)_{\text{SML3}} \rangle$ denotes the canonical ensemble average of the ShiftML3 last layer descriptor. We employ a ridge regressor and fixed regularization strength $\lambda=10$ to obtain ω_{corr} . We split the 19 benchmark crystals into a training set of an increasing number of structures and keep always 4 test structures. Last layer ensemble averaged descriptors as well as averaged ShiftML3 shieldings are obtained from 50 ps PIMD simulations of each crystal at 300K using 32 beads. We repeat the model fitting across 2,000 random splits of the 19 crystals and compare the ShiftML3 thermal average shielding accuracies on the 4 held out structures against the Δ -model corrected values.

DATA AVAILABILITY

We make the curated PET-MOLS training data, and example scripts to rerun the calculations of this work available via a materials-cloud archive associated with this publication made available upon publication.

SUPPORTING INFORMATION

The supporting information is available free of charge upon publication.

CORRESPONDING AUTHORS

lyndon.emsley@epfl.ch
michele.cerioti@epfl.ch

ACKNOWLEDGMENTS

This work has been supported by the Swiss National Science Foundation Grant No. 200020_212046, and by the NCCR MARVEL. M.C. and M.K. acknowledge funding from the European Research Council (ERC) under the research and innovation program Grant Agreement No. 10100189

Supplementary Information for: Quantum-corrected NMR crystallography at scale

Matthias Kellner¹, Ruben Rodriguez-Madrid², Jacob B. Holmes², Victor Paul Principe¹,
Lyndon Emsley^{*2}, Michele Ceriotti^{†1}

¹Laboratory of Computational Science and Modeling, Institut des Matériaux, École Polytechnique
Fédérale de Lausanne, 1015 Lausanne, Switzerland

²Laboratory of Magnetic Resonance, Institut des Sciences et Ingénierie Chimiques, École Polytechnique
Fédérale de Lausanne, 1015 Lausanne, Switzerland

Raw data: All data are available from [xxx]

Contents

S1 Experimental benchmarks for the crystalline solids	13
S1.1 Experimental shifts and predicted shieldings for the ¹ H dataset	13
S1.2 Experimental shifts and predicted shieldings for the ¹³ C dataset	15
S1.3 Experimental shifts and predicted shieldings for the ¹⁵ N dataset	17
S1.4 Parity plots between experimental and predicted shifts for the ¹³ C and ¹⁵ N ex- perimental benchmarks	18
S1.5 Linear Regression	19
S2 GLP-1RA molecular dynamics and PIMD simulations	20
S3 PET-MOLS training details	23
S3.1 Dataset Summary	23
S3.2 Machine learning interatomic potential	23
S4 Evaluation of PET-MOLS	25
S5 Selected atomistic modeling examples with PET-MOLS	26
S5.1 Density of liquid methane	26
S5.2 Equation of state of the benzene crystal	27
S5.3 Radial distribution function of liquid water	27
S5.4 Temperature dependency of ¹ H chemical shieldings in short hydrogen bonded base-acid pairs	29
S5.5 Shielding distribution in succinic acid	30
S6 PET-MOLS Training curve	32
S7 PET-MOLS uncertainty quantification.	33
S8 Learning from experiments: Additional tests	33

*Email: lyndon.emsley@epfl.ch

†Email: michele.ceriotti@epfl.ch

S1 Experimental benchmarks for the crystalline solids

The structures for experimental benchmarks were compiled from Cordova et al¹ for the ¹H dataset while the ¹³C and ¹⁵N datasets of structures were compiled from Ramos *et al.*² These structures were used without further relaxation for chemical shift prediction with ShiftML3³ for the Static-PBE benchmark. As reported, ¹H experimental benchmark are all atoms geometries relaxed using D2 dispersion corrections keeping the cell parameters fixed. The ¹³C and ¹⁵N used the dispersion correction D3(BJ) for geometry optimization of all atoms keeping the cell parameters fixed.

S1.1 Experimental shifts and predicted shieldings for the ¹H dataset

Assigned chemical shift values were used from the previously curated data set.¹ The methyl rotational dynamics were accounted for by averaging the chemical shifts of the three proton positions into a single effective value per methyl group, which was treated as contributing threefold shielding to reflect the three equivalent protons. The same approach is done for magnetically equivalent protons (i.e. methylene groups). In cases of pairwise ambiguities, experimental chemical shifts were resolved by selecting the assignment yielding the lowest shift RMSE. (i.e. H_a and H_b of CH₂ groups)

Table S1: Experimental chemical shifts and ShiftML3 predicted shieldings for the 120 atomic sites in the ¹H benchmark dataset of structures from ShiftML2¹ containing H, C, N, and O elements. Predicted shieldings are given for the Static-PBE, Static-PBE0 geometries, and QNC-NMR ensemble.

Ref. Code	Experimental shift [ppm]	Predicted shieldings [ppm]		
		Static-PBE	Static-PBE0	QNC-NMR
Uracil	7.50	21.99	22.09	22.00
	10.80	18.32	19.10	19.23
	11.20	17.98	19.07	18.78
	6.00	23.99	24.37	23.81
AZD8329	6.92	24.13	24.39	24.04
	8.69	22.30	22.57	22.23
	9.01	21.50	21.55	21.40
	8.47	22.80	23.00	22.71
	15.37	13.65	15.69	15.12
	7.73	22.43	22.66	22.09
	9.64	19.60	20.63	20.07
	2.90	28.11	28.22	27.34
	1.78	28.80	28.93	28.04
	1.88	29.47	29.61	28.69
	1.88	28.47	28.69	27.90
	1.80	28.86	28.97	28.19
	1.60	29.58	29.77	29.00
	0.44	30.29	30.40	29.59
	1.54	29.01	29.16	28.28
	1.88	28.62	28.99	28.36
	1.88	29.54	29.73	28.87
	0.80	29.83	29.97	29.15
	0.80	30.11	30.25	29.32
	1.00	29.17	29.28	28.42
1.74	29.03	29.27	29.09	
1.74	29.75	29.87	28.51	
0.73	30.09	30.32	29.59	
0.73	30.09	30.32	29.59	
0.73	30.09	30.32	29.59	
0.73	29.90	30.11	29.25	
0.73	29.90	30.11	29.25	
0.73	29.90	30.11	29.25	
0.73	30.76	30.92	29.97	
0.73	30.76	30.92	29.97	
0.73	30.76	30.92	29.97	
Naproxen	7.00	23.09	23.27	22.95

Ref. Code	Experimental shift [ppm]	Predicted shieldings [ppm]		
		Static-PBE	Static-PBE0	QNC-NMR
	6.10	24.24	24.33	23.90
	3.80	26.96	27.09	26.32
	4.50	25.69	25.96	25.47
	4.10	25.85	25.96	25.45
	5.90	24.93	25.05	24.63
	3.20	27.73	27.80	26.99
	1.80	29.36	29.59	28.86
	1.80	29.36	29.59	28.86
	1.80	29.36	29.59	28.86
	2.30	28.25	28.46	27.44
	2.30	28.25	28.46	27.44
	2.30	28.25	28.46	27.44
	11.50	16.32	17.39	16.86
Cocaine	3.76	27.01	27.13	26.22
	3.78	27.24	27.53	26.89
	5.63	25.44	25.54	24.8
	3.32	27.33	27.55	26.89
	3.06	28.32	28.46	27.79
	3.49	28.06	28.37	27.66
	2.91	28.98	29.16	28.33
	3.38	28.33	28.54	27.82
	2.56	28.64	28.86	28.11
	2.12	28.97	29.13	28.4
	1.04	29.47	29.66	28.79
	1.04	29.47	29.66	28.79
	1.04	29.47	29.66	28.79
	8.01	22.53	22.74	22.4
	8.01	22.99	23.16	23.05
	8.01	22.79	23.01	22.64
	8.01	22.73	22.94	22.51
	8.01	22.86	23.03	22.68
	3.78	26.81	27.06	26.33
	3.78	26.81	27.06	26.33
	3.78	26.81	27.06	26.33
Theophylline	14.60	14.32	15.30	15.57
	7.70	22.80	22.96	22.31
	3.40	27.49	27.72	27.04
	3.40	27.49	27.72	27.04
	3.40	27.49	27.72	27.04
	3.40	27.49	27.72	27.04
	3.40	27.49	27.72	27.04
	3.40	27.49	27.72	27.04
Atulifapon	1.20	29.32	29.50	28.70
	1.20	29.32	29.50	28.70
	1.20	29.32	29.50	28.70
	10.60	18.11	18.37	18.54
	5.80	23.78	24.02	23.54
	6.90	23.88	23.98	23.61
	7.30	23.06	23.21	22.94
	6.70	24.34	24.54	24.03
	7.00	22.78	22.95	22.56
	3.90	27.01	27.24	26.51
	1.60	28.67	28.83	27.94
	0.00	30.35	30.52	29.65
	1.70	28.55	28.76	27.97
	1.60	29.01	29.35	28.51
	1.60	28.9	29.05	28.38
	-0.50	30.02	30.18	29.23
	0.80	29.51	29.74	28.89
	-0.50	30.57	30.73	29.88
	0.80	29.26	29.42	28.70
	7.70	21.36	21.75	21.30
	7.60	22.58	22.87	22.43
	1.70	29.63	29.68	28.66
	2.70	27.80	27.92	27.24
	6.90	22.46	23.16	22.47
	1.90	28.07	28.22	27.47
	2.70	27.5	27.65	26.96
Dimethylimidazole	4.80	25.91	26.08	25.03
	0.70	29.53	29.68	29.07

Ref. Code	Experimental shift [ppm]	Predicted shieldings [ppm]		
		Static-PBE	Static-PBE0	QNC-NMR
	0.70	29.53	29.68	29.07
	0.70	29.53	29.68	29.07
	1.40	29.41	29.52	28.78
	1.40	29.41	29.52	28.78
	1.40	29.41	29.52	28.78
	13.00	16.30	16.52	16.37
	1.40	29.08	29.25	28.63
	1.40	29.08	29.25	28.63
	1.40	29.08	29.25	28.63
	1.50	28.97	29.12	28.33
	1.50	28.97	29.12	28.33
	1.50	28.97	29.12	28.33
	15.0	14.23	14.32	14.59
	5.20	24.83	25.02	24.40

S1.2 Experimental shifts and predicted shieldings for the ^{13}C dataset

Table S2: Experimental chemical shifts and ShiftML3 predicted shieldings for the 123 atomic sites in the ^{13}C benchmark dataset of structures from Ramos et al.² containing H, C, O and N elements. Predicted shieldings are given for the Static-PBE and Static-PBE0 geometries, and in the QNC-NMR ensemble. The shifts below are ordered according to their appearance in the CIF files.

Ref. Code	Experimental shift [ppm]	Predicted shieldings [ppm]		
		Static-PBE	Static-PBE0	QNC-NMR
ADENOS12	154.10	13.01	16.96	14.61
	147.90	19.54	22.96	20.53
	119.30	46.12	49.53	46.23
	154.70	15.15	18.58	16.26
	137.40	28.15	32.00	28.82
	91.90	75.88	80.18	76.06
	74.60	92.11	96.62	91.84
	70.90	96.01	99.65	95.83
	84.50	81.59	86.42	81.31
	62.50	106.96	110.71	105.16
	ASPARM03	176.40	-12.11	-4.40
51.80		119.42	123.19	117.58
36.10		136.95	138.71	132.38
177.10		-7.22	-1.45	-3.90
FRUCTO02	65.40	102.71	106.29	101.75
	99.70	62.66	68.49	64.79
	67.20	99.59	103.63	98.25
	69.00	99.14	102.26	96.94
	71.40	96.00	100.26	95.76
	64.90	103.54	107.87	102.45
GLUTAM01	173.00	-9.86	-2.60	-5.25
	53.30	115.99	119.55	114.36
	25.50	145.36	147.31	140.82
	28.50	143.23	145.5	139.18
	176.50	-8.84	-3.29	-6.27
GLYCIN29	176.20	-10.94	-3.10	-5.26
	43.50	128.90	131.88	125.87
HXACAN09	133.10	37.49	40.59	36.90
	123.40	46.80	48.36	44.02
	115.70	52.53	53.89	49.49
	152.30	14.47	17.82	14.12
	116.40	51.99	54.69	49.91
	120.60	49.32	50.09	45.58
	169.80	-4.05	2.38	0.31
	23.80	148.73	151.49	144.79
	LALNIN12	176.80	-13.47	-6.29
50.90		119.84	123.30	118.14

Ref. Code	Experimental shift [ppm]	Predicted shieldings [ppm]		
		Static-PBE	Static-PBE0	QNC-NMR
	19.80	154.74	156.18	149.72
LSERIN01	175.10	-10.53	-3.30	-5.17
	55.60	113.87	117.04	112.2
	62.90	104.28	108.14	103.47
LSERMH10	175.60	-12.45	-5.18	-7.19
	58.30	111.98	115.45	110.66
	61.80	106.96	110.44	105.14
LTHREO01	171.90	-5.76	1.06	-1.67
	61.20	110.4	113.34	108.29
	66.80	98.49	103.06	97.48
	20.40	152.89	153.88	148.24
LTYROS11	175.40	-12.34	-5.46	-7.46
	130.30	36.97	39.12	35.22
	116.40	52.18	54.88	50.22
	56.40	114.49	118.10	112.85
	131.00	36.84	38.59	34.53
	118.00	51.96	54.29	49.76
	155.60	11.30	13.51	10.27
	36.80	134.78	136.37	131.19
123.60	44.23	46.32	41.54	
MBDGAL02	105.70	58.04	62.98	58.77
	71.20	97.59	101.10	95.55
	72.10	95.11	98.72	93.61
	69.30	96.52	100.38	96.16
	75.60	89.06	92.43	87.81
	62.80	106.24	109.38	104.07
	57.60	111.18	115.96	109.89
MEMANP11	99.60	64.94	69.80	65.92
	71.30	95.11	98.58	94.42
	71.70	96.10	99.88	94.67
	64.80	102.86	106.79	100.74
	71.90	96.03	100.30	94.72
	58.90	108.85	112.48	106.84
	54.90	113.93	117.81	112.42
MGALPY01	100.40	63.56	69.11	64.54
	67.60	100.43	103.84	98.23
	72.60	93.10	97.25	92.83
	70.00	98.13	101.8	96.63
	72.90	93.84	98.47	93.14
	61.40	106.83	109.99	104.11
	55.20	113.94	118.6	112.39
MGLUCP11	101.00	63.38	68.46	64.25
	72.30	95.72	99.00	93.63
	74.60	93.19	97.33	92.54
	72.50	93.47	97.08	92.73
	75.30	94.69	97.99	92.23
	63.80	105.34	108.77	103.94
	56.50	114.09	117.83	112.51
PERYTO10	50.20	120.38	121.63	116.55
	58.40	109.49	113.29	107.61
RHAMAH12	94.50	71.12	76.61	72.00
	72.20	95.24	99.46	94.68
	71.00	98.13	101.36	95.88
	72.50	95.38	99.57	94.20
	69.80	98.22	102.79	96.92
	17.80	157.07	158.46	153.06
SUCROS04	93.30	71.48	76.68	71.96
	66.00	105.35	107.92	102.46
	73.70	93.45	96.60	91.95
	102.40	52.83	58.93	55.58
	72.80	93.67	98.04	93.08
	82.90	87.08	90.14	85.44
	67.90	99.91	102.93	97.83
	71.80	96.26	99.74	94.79
	73.60	93.69	97.69	92.85

Ref. Code	Experimental shift [ppm]	Predicted shieldings [ppm]		
		Static-PBE	Static-PBE0	QNC-NMR
	81.80	83.50	87.74	83.03
	60.00	108.80	112.51	106.72
	61.00	106.43	110.31	104.38
TRIPHE11	126.40	42.10	44.46	39.51
	129.50	39.33	42.60	39.21
	124.50	44.94	48.22	42.91
	125.90	41.24	43.48	39.28
	127.50	42.78	43.95	39.61
	122.30	48.91	50.37	45.42
	130.20	38.92	40.96	37.80
	129.50	40.70	41.38	38.32
	120.90	50.31	51.58	45.88
	125.90	44.70	44.79	41.16
	121.70	49.19	50.03	45.54
	129.50	40.67	42.14	39.11
	129.50	39.67	41.11	38.05
	122.30	48.50	49.56	45.22
	126.90	41.66	43.18	39.76
	126.90	42.10	43.52	38.90
	123.80	44.47	48.74	44.06
	129.80	40.07	41.03	38.43

S1.3 Experimental shifts and predicted shieldings for the ^{15}N dataset

Table S3: Experimental chemical shifts and ShiftML3 predicted shieldings for the 27 atomic sites in the ^{15}N benchmark dataset of structures from Ramos et al.² containing H, C, O and N elements. Predicted shieldings are given for the Static-PBE and Static-PBE0 geometries, and in the QNC-NMR ensemble.

Ref. Code	Experimental shift [ppm]	Predicted shieldings [ppm]		
		Static-PBE	Static-PBE0	QNC-NMR
BITZAF	249.50	-68.97	-63.21	-65.26
GEHHEH	187.40	11.16	10.26	-16.35
	261.00	-51.89	-57.58	-10.58
GEHHIL	268.50	-81.30	-75.44	-78.68
	261.20	-64.26	-70.35	9.41
LHISTD02	210.80	-30.80	-21.54	-31.93
	132.60	45.81	52.28	43.49
LHISTD13	210.60	-30.58	-21.29	-30.43
	132.40	44.66	51.77	43.14
TEJWAG	143.90	38.03	43.27	32.23
GLYCIN03	-6.50	195.64	198.40	191.73
FUSVAQ01	183.20	-0.19	7.59	-0.60
	174.20	8.87	14.44	7.25
	192.20	-9.81	-0.90	-8.80
	120.20	56.21	62.21	54.01
	50.20	131.18	136.31	131.60
CYTSIN	110.20	65.71	75.81	65.34
	165.20	17.78	23.95	17.84
	54.20	133.13	137.31	130.13
THYMIN01	90.20	83.12	92.46	84.26
	119.20	58.68	65.66	59.07
BAPLOT01	114.70	59.89	68.87	63.62
	72.70	101.92	108.96	104.53
	122.70	53.71	63.69	54.66
	178.70	1.61	8.30	0.27
URACIL	96.20	75.63	84.57	77.11

Ref. Code	Experimental shift [ppm]	Predicted shieldings [ppm]		
		Static-PBE	Static-PBE0	QNC-NMR
	120.20	59.00	65.34	58.21

S1.4 Parity plots between experimental and predicted shifts for the ^{13}C and ^{15}N experimental benchmarks

In Figure S1 there are the parity plots for the ^{13}C experimental benchmark from Ramos et al.² using the linear fit to map the experimental chemical shifts against calculated shieldings with a slope of -1. As discussed in the main text, the Static-PBE0 geometries using the PET-MOLS led an improvement of the accuracies of the 28% (2.68 to 1.92 ppm) with respect to the Static-PBE geometries. An improvement of 32% (2.68 to 1.83 ppm) is further achieved with the new proposed QNC-NMR protocol.

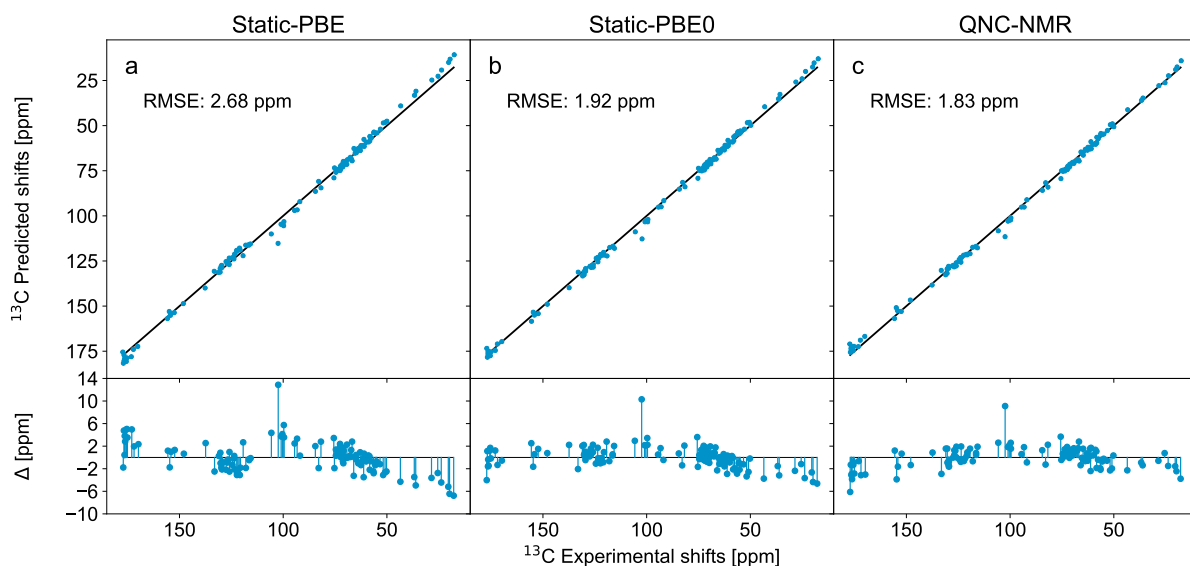


Figure S1: Comparison of experimental and predicted ^{13}C chemical shifts computed with ShiftML3, using Static-PBE optimized geometries (a), Static-PBE0 optimized geometries (b), and the QNC-NMR protocol (c). The black diagonal line in each panel corresponds to a perfect correlation. The accuracy of the predictions is evaluated with the root-mean square error (RMSE). On the lower panels, Δ is the difference between the predicted and the experimental chemical shift ($\Delta = \delta_{pred} - \delta_{exp}$).

In Figure S2, the ^{15}N experimental benchmark are show for the three approaches. Prediction of Static-PBE0 optimized geometries and using the QNC-NMR protocol employing the PET-MOLS improves the predictions by 30% (3.92 ppm) and 24% (4.30 ppm), respectively, with respect to the Static-PBE geometries (5.63 ppm).

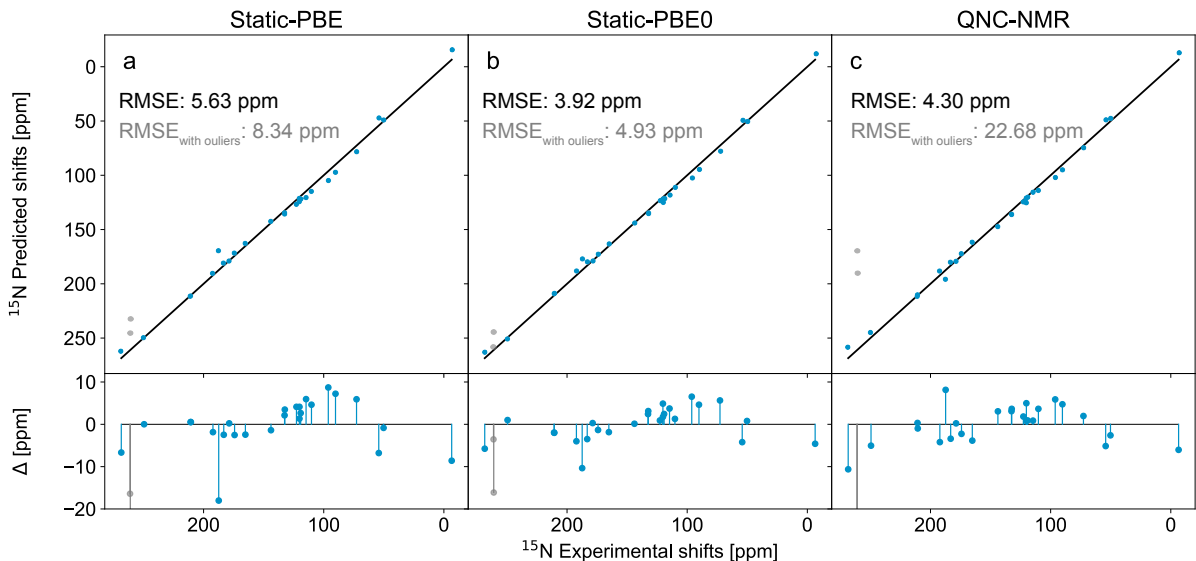


Figure S2: Comparison of experimental and predicted ^{15}N chemical shifts computed with ShiftML3, using Static-PBE optimized geometries (a), Static-PBE0 optimized geometries (b), and the QNC-NMR protocol (c). The black diagonal line in each panel corresponds to a perfect correlation. The accuracy of the predictions is evaluated with the root-mean square error (RMSE) without (in black) and with the outliers (in grey). On the lower panels, Δ is the difference between the predicted and the experimental chemical shift ($\Delta = \delta_{pred} - \delta_{exp}$). Outlier local atomic environments not included in the fitting are displayed in color grey. Those correspond to the structures GEHHIL and GEHHEH whose Schiff base motifs have highly uncertain protonation state and are discussed in more detail the main text.

S1.5 Linear Regression

For the analysis, a linear regression $\delta = a\sigma + b$ with a slope of $a=-1$ and intercept (b) fit to give best agreement between predicted shielding (σ) and experimental chemical shift (δ) were used. For completeness, we have included regression parameters where the slope is also optimized. These optimized parameters are listed in Table S4.

In Tables S1-S3 there is all data used for the mapping of the experimental shifts as a function of the predicted shieldings. All local atomic environments are considered for all three experimental benchmark, except the two ^{15}N sites corresponding to the Schiff base sites. The reason of excluding those sites is the sensitivity to the protonation state encoded in the QNC-NMR protocol and it is further discussed in the main text.

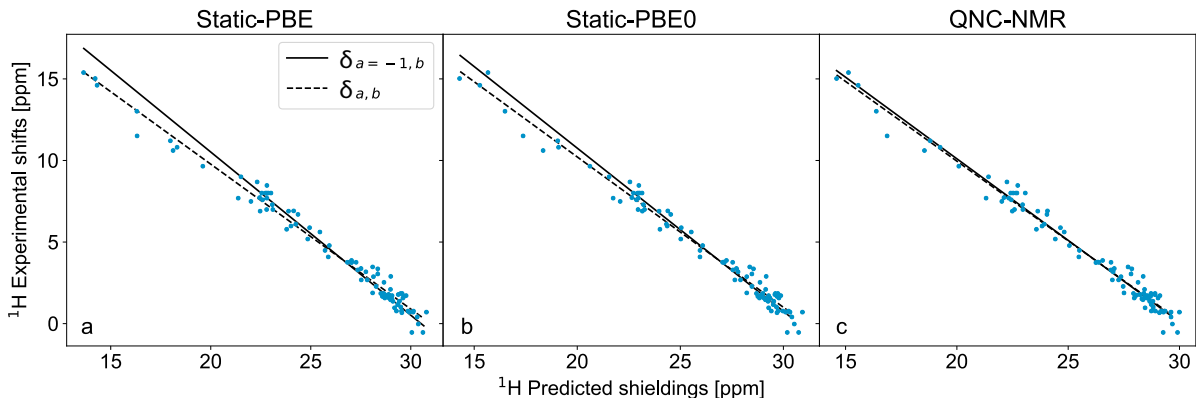


Figure S3: ^1H experimental chemical shifts as a function of the ShiftML3 predicted shieldings for the Static-PBE optimized geometries (a), Static-PBE0 optimized geometries (b), and the QNC-NMR protocol (c). In a black solid line ($\delta = a\sigma + b$) is the fitted linear regression keeping the slope fixed ($\delta_{a=-1,b}$, used in the main text); and in black dashed line ($\delta_{a,b}$) is the linear fit optimizing both the slope and intercept.

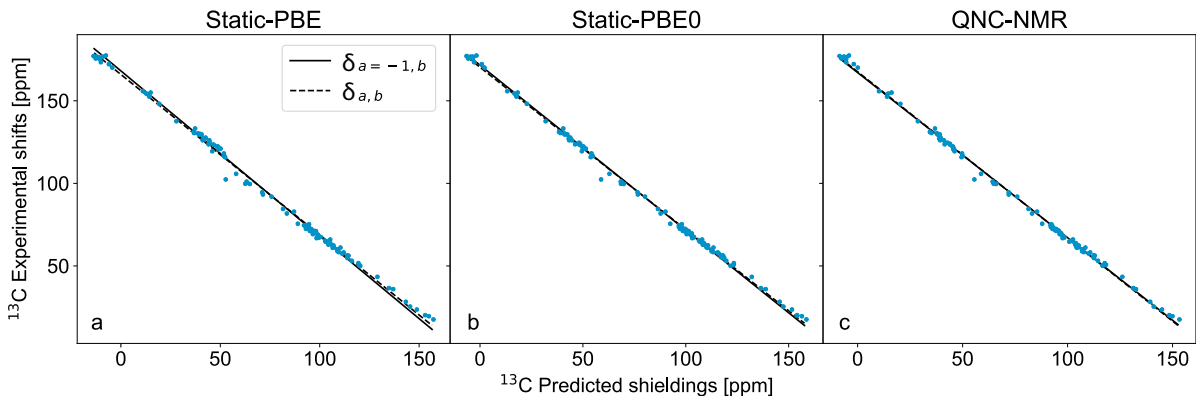


Figure S4: ^{13}C experimental chemical shifts as a function of the ShiftML3 predicted shieldings for the Static-PBE optimized geometries (a), Static-PBE0 optimized geometries (b), and the QNC-NMR protocol (c). In a black solid line ($\delta = a\sigma + b$) is the fitted linear regression keeping the slope fixed ($\delta_{a=-1,b}$, used in the main text); and in black dashed line ($\delta_{a,b}$) is the linear fit optimizing both the slope and intercept.

S2 GLP-1RA molecular dynamics and PIMD simulations

The chlorine atoms in original structure (1-Cl) have been mutated to either a hydrogen(1-H), cyano (1-CN), or methyl (1-Me) for the 17 selected MD frames.

For the case of the 1-H mutation, the Cl were replaced by projecting the new hydrogen along the original C-Cl bond vector and rescaling that vector to 1.09 Å, the standard C-H bond length.

For the 1-CN mutation, the same procedure used for the Cl→H substitution was applied to define the bond vector. The chlorine atom was replaced by the cyano carbon, which was positioned 1.47 Å from the parent atom along the original C-Cl bond direction, consistent with typical C(sp)-C(sp²) bond lengths. The terminal nitrogen was then placed an additional 1.16 Å along the same vector, yielding a linear C≡N group with a physically reasonable triple-bond distance.

For the 1-Me mutation, the chlorine atom was replaced by a methyl carbon positioned 1.53 Å from the parent atom along the original C-Cl bond vector; three hydrogens were then placed

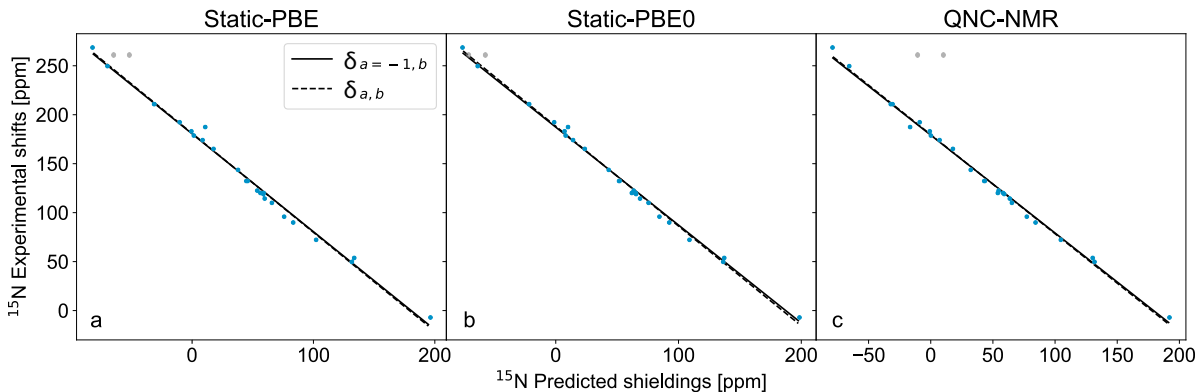


Figure S5: ^{15}N experimental chemical shifts as a function of the ShiftML3 predicted shieldings for the Static-PBE optimized geometries (a), Static-PBE0 optimized geometries (b), and the QNC-NMR protocol (c). In a black solid line ($\delta = a\sigma + b$) is the fitted linear regression keeping the slope fixed ($\delta_{a=-1,b}$, used in the main text); and in black dashed line ($\delta_{a,b}$) is the linear fit optimizing both the slope and intercept. Outlier local atomic environments not included in the fitting are displayed in color grey. Those correspond to the structures GEHHIL and GEHHEH whose Schiff base motifs have highly uncertain protonation state and are discussed in more detail in the main text.

Table S4: Linear fitting parameters (slope, a ; and intercept, b) for the three different benchmarks (^1H , ^{13}C and ^{15}N) of crystalline structures using the Static-PBE geometries, the Static-PBE0 geometries, and the QNC-NMR protocol. Both approaches in the fitting — keeping the slope fixed to -1 and fitting the intercept, and fitting both the slope and intercept — are considered with their respective values and RMSE (root-mean square error).

Nuclei	Method	Fix slope ($a = -1$)		Fit slope		
		b	RMSE [ppm]	a	b	RMSE [ppm]
^1H	Static-PBE	30.52	0.66	-0.8882	27.54	0.50
	Static-PBE0	30.76	0.57	-0.9217	28.65	0.48
	QNC-NMR	30.11	0.50	-0.9768	29.50	0.50
^{13}C	Static-PBE	168.10	2.68	-0.9708	165.93	2.38
	Static-PBE0	171.63	1.92	-0.9830	170.30	1.78
	QNC-NMR	167.08	1.83	-1.0070	167.60	1.81
^{15}N	Static-PBE	180.54	5.63	-1.0103	180.96	5.60
	Static-PBE0	187.30	3.92	-1.0188	188.19	3.74
	QNC-NMR	179.19	4.30	-1.0111	179.63	4.24

at 1.09 \AA from the methyl carbon with ideal tetrahedral geometry (109.5°) and 120° rotational spacing about the C-C axis.

For each mutation, a geometry optimization (Static-PBE0 geometry) was performed where no significant molecular rearrangement was observed with respect to the original FF-MD. The averaged root-mean square displacement was $0.04 \pm 0.01 \text{ \AA}$ (excluding the mutated sites) for all mutants. This is highlighted further in Figure S6, where the carboxylic acid hydrogen bonds are unperturbed. Overall, the largest deviation is from the lengthening of the OH bond. We note, that reduction of None for the 1-CN mutation which is 0.92% (50 structures).

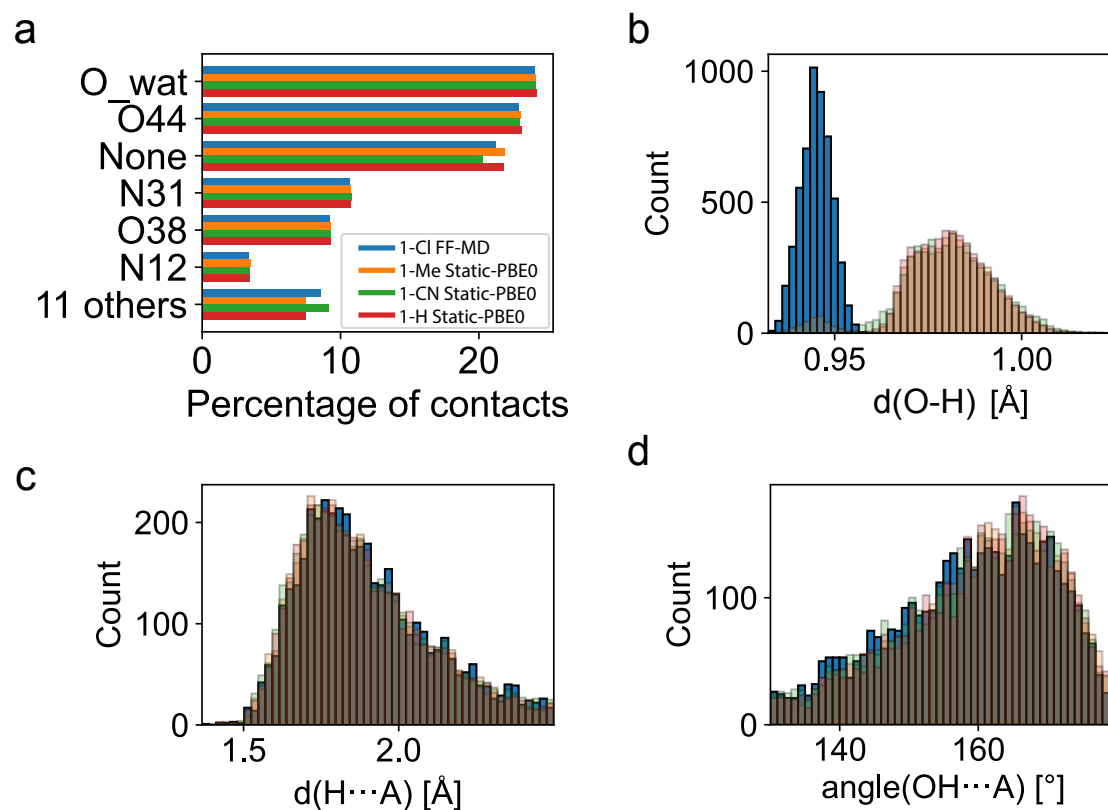


Figure S6: Static-PBE0 geometry optimization on the selected MD frames on the geometric features related to the acidic H42 proton. (a) Occurrence of different H-bond acceptors for H42 for the different 17 mutated MD frames geometry relaxed using the PET-MOLS (1-Me in orange, 1-CN in green, and 1-H in red) and the original 1-Cl (in blue). H-bond donors are considered to have H-bonds when the angle between $\text{OH}\cdots\text{X}$ is $180\pm 50^\circ$, and the $\text{H}\cdots\text{A}$ distance is less than 2.5 \AA . (b) The OH bond distance for all candidates. (c) The distance between H42 and acceptor for all API molecules involved in hydrogen bonding. (d) The $\text{O-H42}\cdots\text{A}$ angle for all API molecules involved in hydrogen bonding.

After geometry relaxation, the structures were equilibrated with NVT MD for about 200 ps at 300K and the subsequent 2ps PIGLET-accelerated-PIMD simulation using 8-beads, employing the PET-MOLS in both simulations. In Figure S7, we show the averaged acidic H42 chemical shifts along the trajectories for both simulations.

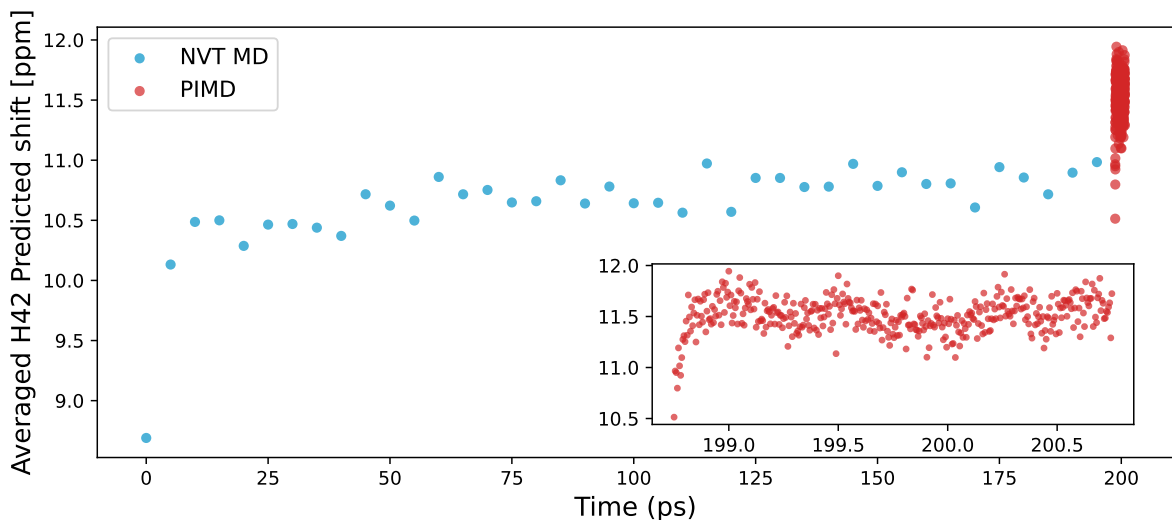


Figure S7: The averaged H42 predicted chemical shift through the NVT MD (in blue) and PIMD (in red) simulation timestep for one of the 17 MD frames. The inset is a zoomed-in region of averaged H42 predicted shift along the PIMD simulation.

S3 PET-MOLS training details

S3.1 Dataset Summary

In Figure S8 we show the distribution of selected properties of the PBE0+MBD reference dataset computations that we introduce in this work and use to train PET-MOLS. Table S5 lists the number of unique compositions, structures and total number of atoms in the training, validation and test sets used to train and evaluate PET-MOLS.

Table S5: Number of unique compositions $N_{\text{compositions}}$, number of structures $N_{\text{structures}}$ and total number of atoms N_{atoms} in training, validation and test set used to train PET-MOLS.

Set	$N_{\text{compositions}}$	$N_{\text{structures}}$	N_{atoms}
Training	2013	10056	900568
Validation	56	280	26130
Test	168	840	71145

S3.2 Machine learning interatomic potential

We construct the PET-MOLS machine learning potential based on the point-edge transformer architecture (PET) from Podznyakov and Ceriotti.⁴ Model hyperparameters were taken from a hyperparameter search from the PET-MAD project, a universal MLIP based on the PET architecture,⁵ that aimed to find optimal model hyperparameters balancing evaluation cost and prediction accuracy of PET models trained on large datasets (see also supplementary Figure 1 in Ref.⁵). Model hyperparameters were adopted without further optimization. The training dataset of PET-MAD contained also a portion of organic crystals, albeit computed at the PBEsol GGA DFT level of theory and we expect a good transferability of the PET-MAD hyperparameters to PET-MOLS trainings. PET-MOLS was trained for 3000 epochs in total. For the creation of a training set, the portion of structures containing only elements H,C,N,O from the ShiftML2/3 training and test databases were selected. Originally these molecular compositions were selected via farthest point sampling (FPS) from the Cambridge Structural Database (CSD) to cover a

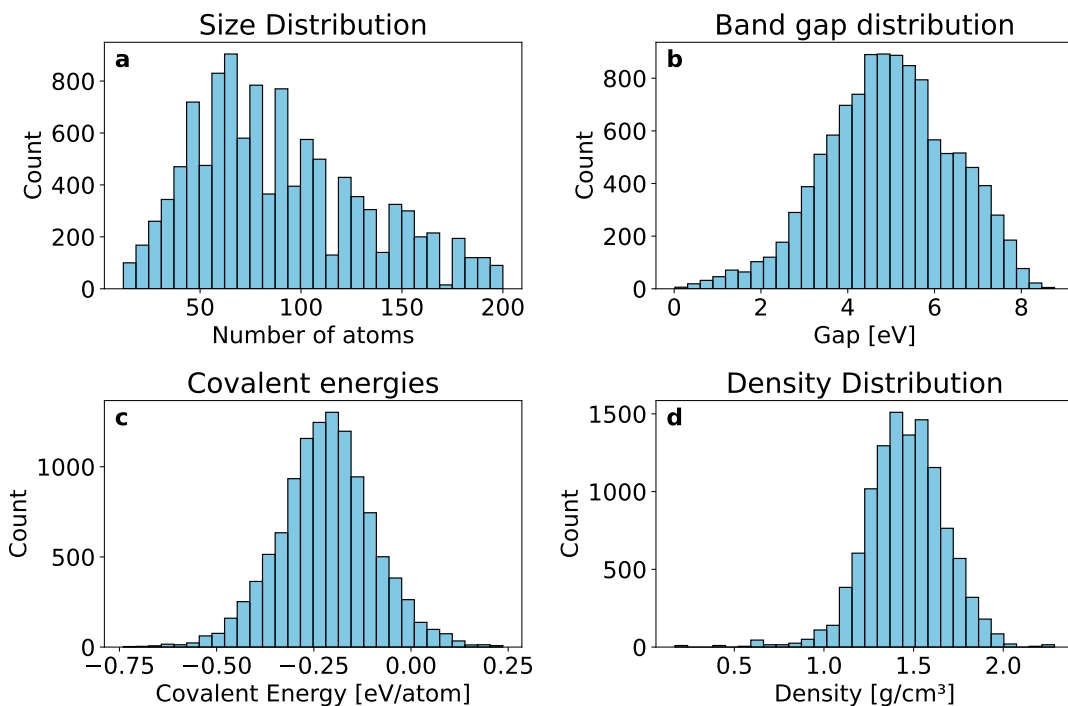


Figure S8: Distribution of properties of the joint training, validation and test sets. Panel (a) shows the distribution of atoms per structure, panel (b) shows the distribution of electronic band gaps, panel (c) the distribution of covalent energies and panel (d) shows the distribution of densities of the joint datasets.

broad range of structural motifs. The pool of candidates of the CSD.-sampled database was limited to structures containing up to 200 atoms to restrict memory and computational costs of reference computation. Experimental crystal structures were geometry relaxed using PBE-D2 and for each unique composition four thermally distorted structures were generated from short molecular dynamics simulations at 300 K using PBE-D2. A total of 2,237 unique compositions was taken from the ShiftML2/3 dataset, forming together with the thermally distorted structures a dataset containing 11,176 structures. The dataset was split into a training, validation and testing set along compositions, assigning the relaxed and thermally distorted structures of one compositions exclusively to either set in order to evaluate the capabilities of PET-MOLS against unseen compositions and their distorted structures. We train PET-MOLS on a dataset of 2,013 unique organic crystal compositions with a total of 10,056 training structures. A validation set of 56 unique compositions with 280 structures is used for the learning rate scheduler during training. Prediction errors are evaluated on a test set containing 168 unique compositions with 840 structures. Training curves of PET-MOLS are shown in the SI Fig. S18. A more detailed analysis of the properties of PET-MOLS is discussed in the following sections.

S4 Evaluation of PET-MOLS

We evaluate PET-MOLS predictions of the covalent energy E_{cov} on a test set containing 840 structures of 168 unique compositions. The covalent energy is defined by removing isolated atom energies ϵ^{ref} from the potential DFT/MLIP predicted energies V_{pot} :

$$E_{\text{covalent}} = V_{\text{pot}} - \sum_{j \in (H,C,N,O)} n_j \epsilon_j^{\text{ref}} \quad (1)$$

Note that composition energies are removed by a least squares fitted composition model in PET-MOLS and the total prediction errors on total potential energies V_{pot} and E_{cov} of PET-MOLS are identical modulo floating point errors, but the standard deviations of V_{pot} would be artificially enlarged given that isolated atom energies can be significantly larger than covalent energies making the normalized RMSE error seem artificially low when they are not removed. Fig. S9 (a) shows parity plots of predicted and computed covalent energies. Panel (b) shows the prediction errors of covalent energies ($\Delta E_{\text{covalent}}$) against the range of total covalent energies, highlighting that there are no biases in prediction errors towards particularly small or large covalent energies.

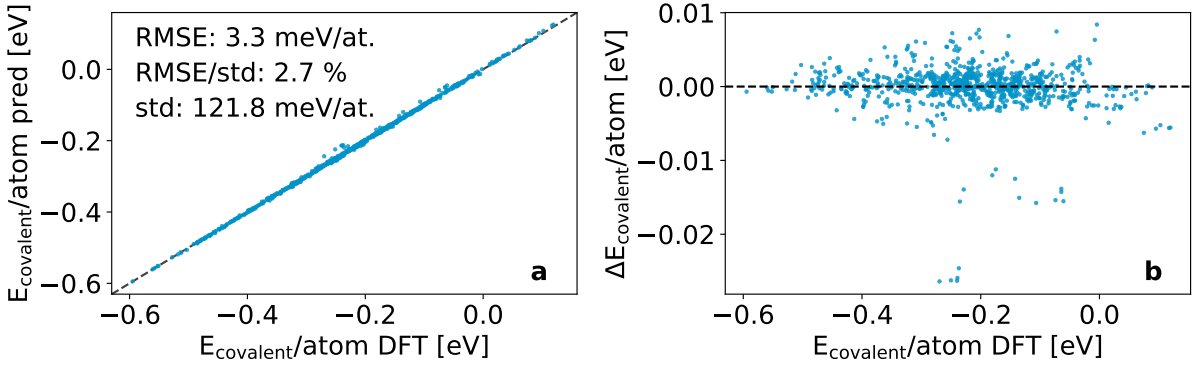


Figure S9: Parity plots of DFT covalent energy against predicted covalent energies by PET-MOLS (a) and DFT covalent energies against covalent energy prediction errors between PET-MOLS and DFT. Note the different x and y scales.

We also evaluate the force prediction errors of PET-MOLS against DFT prediction errors and show parity plots of the PET-MOLS against DFT forces in Fig. S10.

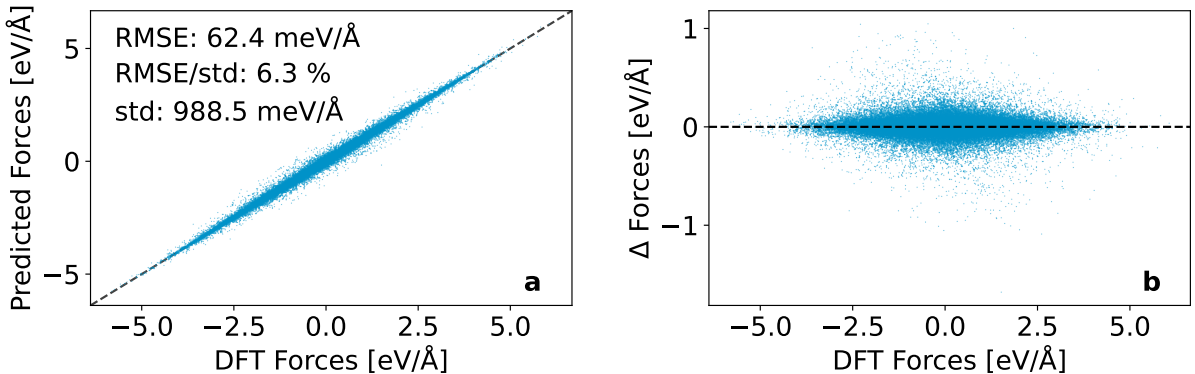


Figure S10: Parity plots of DFT force components against predicted forces by PET-MOLS (a) and force prediction errors between PET-MOLS and DFT against DFT forces.

S5 Selected atomistic modeling examples with PET-MOLS

We evaluate PET-MOLS on selected modeling problems in condensed organic matter, that profit from both incorporation of quantum nuclear effects as well as first principle quality models of the potential energy surface. We used PET-MOLS to compute the density of liquid methane at high pressure, the equation of state (EOS) and average molecular volume of a benzene crystal Form 1, the radial distribution functions of liquid water, the temperature dependency of proton chemical shieldings in the organic acid-base pair SEDJUI and finally we use the chemical shielding distribution of acid protons in succinic acid to test the quantitative agreement of PET-MOLS with bespoke models built for succinic acid.

S5.1 Density of liquid methane

We compute the density of liquid methane with PIMD simulations with PET-MOLS. Veit and coworkers computed the equation of state of liquid methane using bespoke gaussian approximation potentials (GAP),⁶ revealing a strong sensitivity of the bulk density towards the parametrization of the van der waals interactions. Additionally, Pereyaslavets and coworkers found a non-negligible sensitivity of the bulk density of short alkanes towards nuclear quantum effects.⁷ Veit and coworkers computed bulk densities with PIMD to account for such effects. We choose to adopt Veit’s and Coworkers simulation parameters, simulating boxes of 100 methane molecules using colored Noise GLE barostats with coupling times of 100 fs and PIGLET thermostat with 16 beads, employing a timestep of 0.5 fs.^{8,9} Periodic systems are first equilibrated with short simulations in the NVT ensemble and then production simulations are run in the NPT ensemble. We simulate the methane system for a total of 250 ps. We find that the average density of PET-MOLS methane at 188 K and 278 bar is $0.355 \pm 0.002 \text{ g/cm}^{-3}$ which is in excellent agreement with the experimental values found to be 0.350 g/cm^{-3} at the identical conditions.¹⁰ Sampling uncertainties were computed by blocking analysis splitting the trajectory into 10 blocks. In Fig S11 we show the time-evolution of the density of the simulation box.

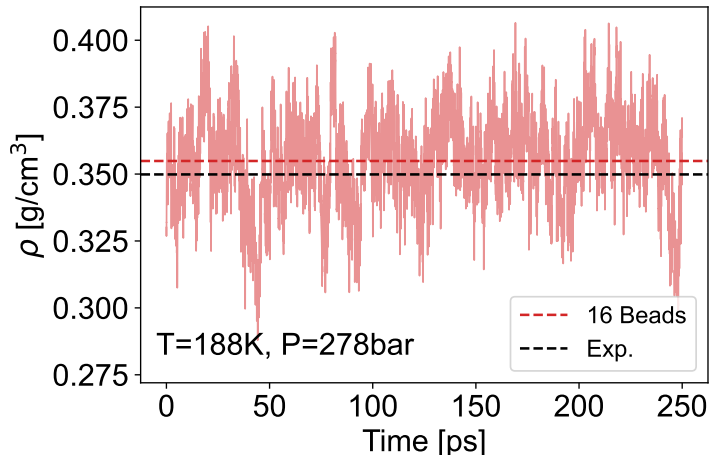


Figure S11: Path integral molecular dynamics simulations of liquid methane using PET-MOLS at 188 K at 278 bar. We show the time-evolution of the box density of the PIMD simulation.

S5.2 Equation of state of the benzene crystal

We compute the equation of state (EOS) of the benzene crystal using PET-MOLS and compute the average molecular volume of deuterated benzene C6D6 form I crystals in order to compare them with neutron scattering experiments of C6D6 performed at 123 K.¹¹ The EOS values are obtained from Murnaghan equation of state fits in order to compare them with computational values from.^{12,13} In order to compute finite temperature average volumes of C6D6 we performed PIMD-NPT simulations with PET-MOLS at 123 K and 1 Bar using 16 Beads for 100 ps, employing a timestep of 0.5 fs, a PIGLET thermostat, and a colored noise barostat and isotropic cell for barostating. We find that the average molecular volumes of C6D6 computed from PIMD simulation amounts to 116.7 Å³ per molecule which is in good agreement with the experimental values of 118.3 Å³ per molecule.¹¹

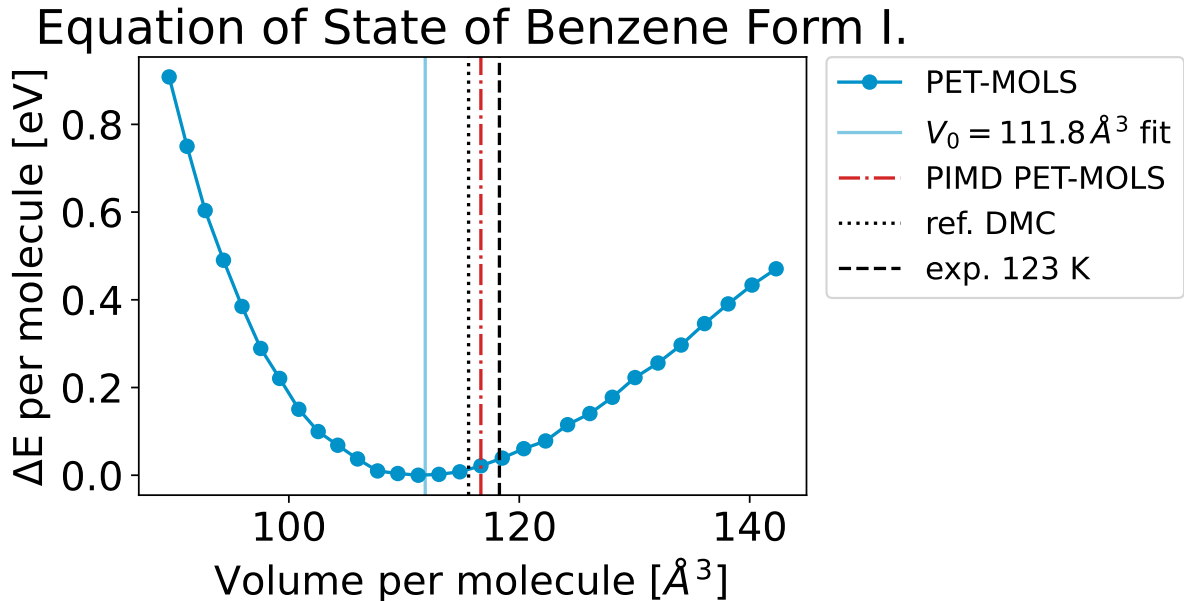


Figure S12: Equation of state (EOS) of benzene form I using PET-MOLS. Additional molecular volumes of C6D6 PIMD averages at 1 bar and 123 K are shown for comparison, as well as experimental neutron scattering values at 123K¹¹ are indicated and static values of a diffusion quantum Monte Carlo (DMC) computation.¹³

S5.3 Radial distribution function of liquid water

We compute radial distribution functions $g(r)$ of liquid water using PIMD simulations and PET-MOLS. It is well known, that simulating radial distribution functions of liquid water require both an accurate description of the inter- and intramolecular interactions^{14–16} as well as the inclusion of NQEs.^{17–19} We note that in the construction of PET-MOLS, structures containing only water were not included in the training set. Water within the training set is present in the crystalline hydrates. We compute the element-wise radial distribution functions from NPT-PIMD simulations of boxes of 256 H₂O molecules at 390 K, compensating for the overestimated melting point of the PET-MOLS and compare them with experimentally measured radial distribution functions at 298 K.²⁰ We perform molecular dynamics using a PIGLET thermostat with 6-beads for 250 ps and 1 bar external pressure, employing a timestep of 0.5 fs. Even though the study of liquid water constitutes a clear out-of-distribution example for PET-MOLS we find that the radial distribution functions of the PET-MOLS water model are in acceptable agreement with the experimental radial distribution functions at 300 K. In Figure S13 we compare computed

and experimental radial distribution functions.

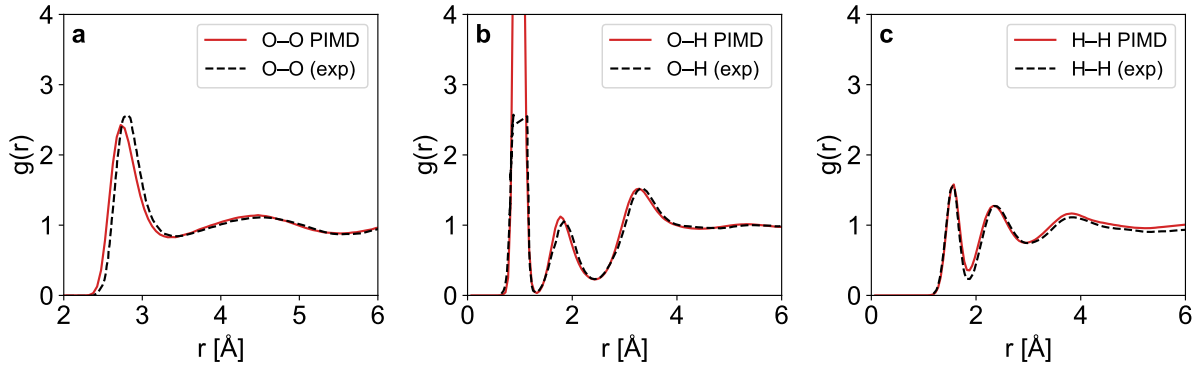


Figure S13: (a) Oxygen-Oxygen RDF , (b) Hydrogen-Oxygen RDF and (c) Hydrogen-Hydrogen RDF of liquid water PIMD simulations with PET-MOLS at 390 K.

In Figure S14 we compare RDF and mean squared displacements (MSD) of Oxygen for liquid water at variable simulation temperatures. From 390K to 360K, we observed a significantly lower MSD and decrease in oxygen-oxygen RDF values between coordination shells, confirms that below 390 K the water must be considered undercooled.

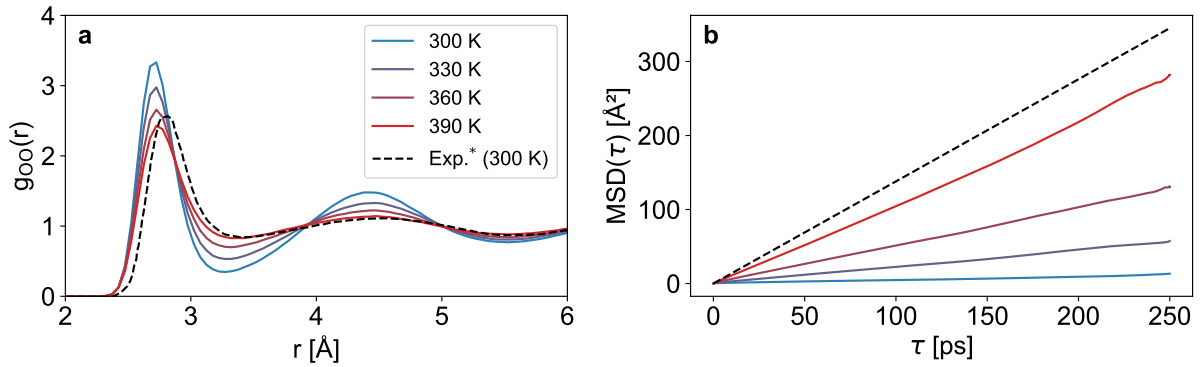


Figure S14: Oxygen-Oxygen RDF of PIMD simulations of PET-MOLS for variable temperatures (a), and mean squared displacements (MSD) of oxygen of the same simulations (b). Note that the experimental oxygen MSD values at 300 K are computed from experimental diffusion coefficients. Computed diffusion coefficients have not been corrected for finite size effects and are influenced by the coloured-noise thermostat and should be regarded as a crude measure for the viscosity of the PET-MOLS water model at varying temperatures.

S5.4 Temperature dependency of ^1H chemical shieldings in short hydrogen bonded base-acid pairs

We compute the temperature-dependency of ^1H chemical shifts in the organic co-crystal system SEDJUI. Štoček and coworkers identified a particular sensitivity of acidic ^1H shifts in molecular crystals with short hydrogen bonds to quantum nuclear effects.²¹ In the system SEDJUI (3-methyl-4-nitrophenol and 4-dimethylaminopyridine) the finite temperature effects and NQEs affect the fractional protonation states strongly and over a temperature range of 173 K to 373 K a conversion of salt to cocrystal is observed, as confirmed by ^1H NMR shifts of acidic protons. We probe the temperature sensitivity of acid ^1H shifts in SEDJUI models and run PIMD dynamics with PET-MOLS of SEDJUI structures. We run molecular dynamics for 150 ps at each temperature in the NPT ensemble at 1 bar pressure with an isotropic cell. We use a PILE-L thermostat for thermostating and a coupling time of 100 fs, as well as a langevin barostat with a coupling time of 100 fs. All simulations use 32 replicas and a timestep of 0.5 fs. We compute chemical shielding averages from the simulation trajectories with ShiftML3. Computed chemical shielding averages are converted to chemical shifts using a fixed regression slope of $a = -1$ and intercept of $b = 30.11$. In Figure S15 we show the temperature dependency of both PIMD simulated chemical shifts and experimentally measured values. Note that unlike in the main text, in which we compare only relative chemical shift differences $\Delta\sigma_{\text{iso}}$ to the chemical shifts at 173 K, we visualize in this additional figure the total chemical shift (after regression with fix slope and QNC-NMR offset), highlighting that the temperature dependency is captured exactly, whilst the absolute chemical shift value deviates by about 0.5 ppm which is in line with the prediction accuracy of ^1H chemical shifts by QNC-NMR against experimental benchmark structures. This deviation can most probably be attributed to shortcomings in the reference GIPAW DFT calculations in the ShiftML3 training database.

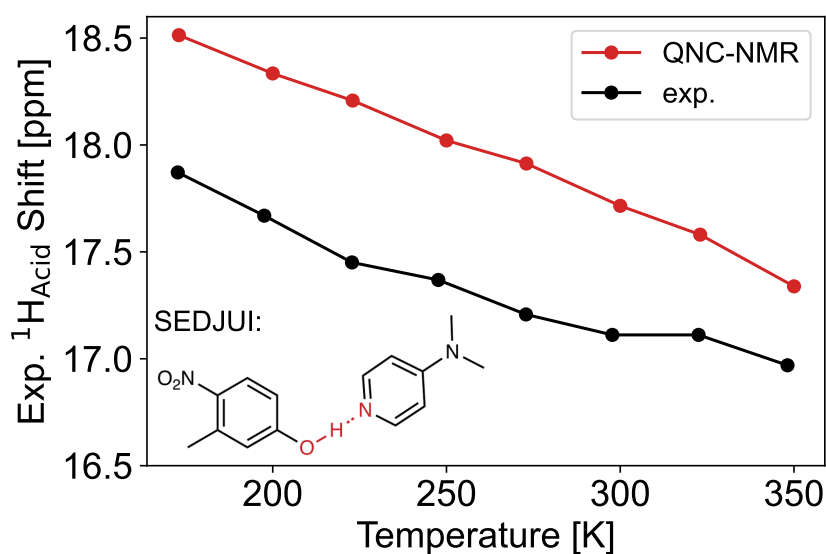


Figure S15: Temperature dependency of the ^1H chemical shifts of acidic protons of the SEDJUI cocrystal system, computed from PIMD simulations and experimental reference values from Ref.²¹

S5.5 Shielding distribution in succinic acid

We evaluate our QNC-NMR protocol (PET-MOLS and ShiftML3) against a computational model to assert that the introduction of surrogate models that enable QNC-NMR in the first place does not introduce biases in the computation of shieldings and ensemble averages of shieldings, with respect to the reference electronic structure methods employed for shielding computations and the potential energy surface. Unfortunately, even for the smallest of systems, computing thermodynamic averages of observables using ab initio molecular dynamics at the PBE0+MBD level of theory as well as computing chemical shieldings from the structural ensemble generated by PIMD, becomes prohibitively expensive. Instead, we train "bespoke" machine learning models that have improved prediction accuracies for both potential energy predictions and shieldings, by training on datasets curated for the purpose of generating highly accurate surrogate models for one specific system, effectively setting up a bespoke QNC-NMR workflow for one specific system. We choose to study the ^1H chemical shielding distributions in α -succinic acid as the reference system. Engel and coworkers, have studied the shielding distributions of acidic protons in succinic acid by means of bespoke MLIPs and chemical shielding models.²² The reference DFT computations for their MLIPs were used employing identical PBE0+MBD parameters (FHI-AIMS, medium basis) enabling us to directly compare the potential energy prediction accuracies of PET-MOLS against a densely sampled reference set of DFT computations of succinic acid structures. For chemical shielding predictions we use a linear-SOAP model that we refitted on an additional set of GIPAW-PBE reference computations that were introduced by Engel et al. to build a bespoke chemical shielding model for succinic acid, with comparable ^1H prediction accuracies as the reference kernel model, presented in the original work of Engel.^{5,22} We construct a bespoke MLIP for succinic acid, by Low-Rank Adaptation (LORA) finetuning²³ PET-MOLS on a dataset of 1800 training configurations of succinic acid computed at the PBE0+MBD level of theory. We refer to this model as LORA-PET-MOLS. Prediction accuracies of bespoke shielding models and MLIP as well as PET-MOLS are listed in Table S7. Prediction accuracies of the bespoke chemical shielding model and ShiftML3 are listed in Table S8. We show parity plots of ShiftML3 predicted chemical shieldings on a test set of 177 succinic acid configurations and predictions from the bespoke chemical shielding model against GIPAW reference calculations in Fig. S17. Dataset sized for both training a chemical shielding and MLIP model are summarized in Table S6. The datasets were obtained by generating a large number of thermally distorted configurations of α and β polymorphs of crystalline succinic acid. More details about the training set generation can be found in the original publication Ref.²² As expected, we find that both bespoke MLIPs and shielding models are more accurate against reference DFT calculations - Fig S16 we compare ^1H chemical shielding distributions computed by either bespoke chemical shielding models or ShiftML3, furthermore we compare distributions of chemical shieldings obtained from PIMD simulations employing the finetuned MLIP or the general PET-MOLS. We perform NVT-PIMD molecular dynamics for 250 ps at 300 K with a timestep of 0.5 fs, using a PILE-L langevin thermostat for thermostating with a coupling time of 100 fs. We find computed thermodynamic averages of acidic proton shieldings between ShiftML3/PET-MOLS simulations and bespoke models to be in excellent agreement and only differ by 0.07 ppm, justifying the use of universal MLIPs and chemical shielding models for the computation of thermodynamic averages of chemical shieldings.

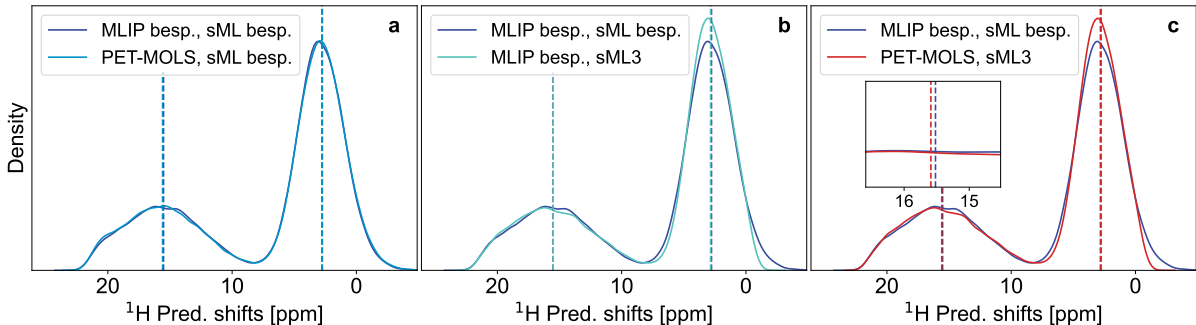


Figure S16: (a) ^1H chemical shielding distributions computed by bespoke shielding models, but generating the ensemble of structures using either a bespoke MLIP or PET-MOLS, (b) using the bespoke MLIP to generate an ensemble of structures but computing shieldings with either bespoke or general ShiftML3 chemical shielding model and finally (c), comparing distributions using either entirely bespoke models for structure generation and shielding computations, or the general ShiftML3 and PET-MOLS models, effectively comparing the general QNC-NMR protocol with a fully bespoke one for succinic acid. Dashed lines correspond to averaged shift values of acidic and aliphatic protons in succinic acid.

Table S6: Summary of Succinic acid datasets used to train bespoke chemical shielding models and MLIPs. We list the number of succinic acid configurations, for which shieldings (GIPAW-PBE) or energies and forces (PBE0+MBD) have been computed, in training set n_{train} , validation set n_{val} and test set n_{test} .

Ref. Theory	n_{train}	n_{val}	n_{test}
PBE0+MBD	1800	200	200
GIPAW-PBE	1450	93	177

Table S7: Evaluation metrics of the LoRA-PET-MOLSfinetuned model and PET-MOLS on a testset of 200 distorted succinic acid configurations computed at the PBE0+MBD reference level.

Models	E MAE/at. [meV/at.]	E RMSE/at. [meV/at.]	F MAE [meV/Å]	F RMSE [meV/Å]
PET-MOLS	1.10	1.34	23.01	88.94
LoRA-PET-MOLS	0.65	0.80	27.95	37.38

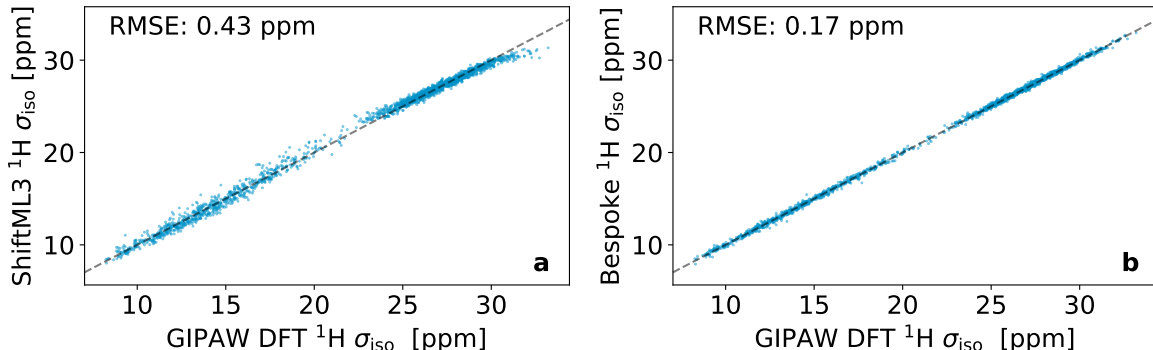


Figure S17: Parity plots of ^1H chemical shielding predictions of ShiftML3 (a) and from a bespoke machine learning model (b) against reference GIPAW DFT shielding computations.

Table S8: Evaluation metrics of ^1H isotropic chemical shieldings predicted by ShiftML3 and a bespoke machine learning model on a testset of 177 distorted succinic acid configurations computed at the GIPAW-PBE level of theory.

Models	^1H σ_{iso} MAE [ppm]	^1H σ_{iso} RMSE [ppm]
ShiftML3	0.32	0.43
Bespoke	0.11	0.17

S6 PET-MOLS Training curve

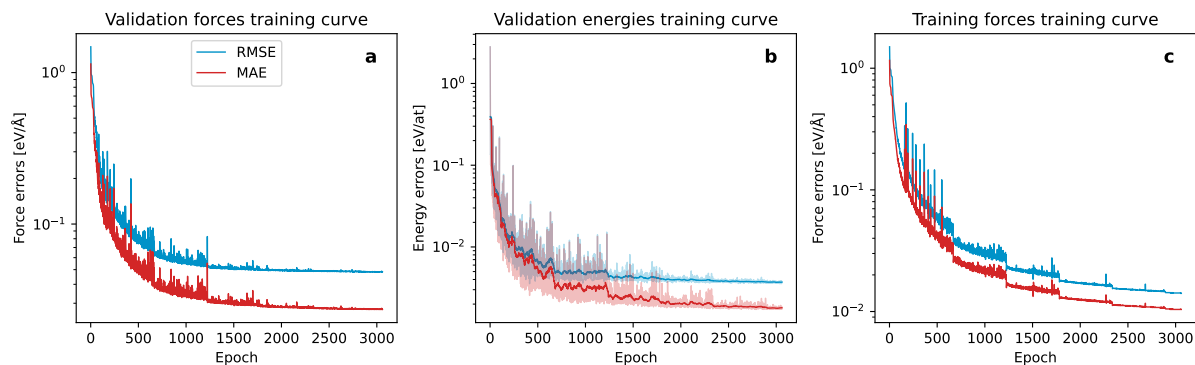


Figure S18: (a) Validation forces and (b) energy error metrics (MAE and RMSE) training curves against epoch number as well as (c) force training set evaluation error, training curve.

S7 PET-MOLS uncertainty quantification.

We equip PET-MOLS with an uncertainty estimator of its potential energy predictions. We use the last-layer prediction rigidity approach, which is a last layer Laplace approximation to the neural network weight posterior.²⁴ We then sample an ensemble of last layer weights, from the approximated last layer posterior. Last layer ensembling has been proven effective for the uncertainty quantification of atomistic simulation, particularly for cases in which the neural network predictions of the potential energy $V_{\text{NN}}(A)$ for a structure, needs to be propagated to an arbitrary function $f(V_{\text{NN}}(A))$ (for example the thermodynamic averages of chemical shieldings).²⁵ We find that a double logarithmic plot, in which we plot predicted potential energy uncertainties against unsigned prediction errors on some hold out test set, provides a valuable visual aid to assess the quality of uncertainty estimators. In Figure S19 we present such a plot of the PET-MOLS predicted uncertainties (the standard deviation of the PET-MOLS committee energy predictions) against the unsigned prediction errors. For more information how to interpret these plots, please also consult References.^{24,25}

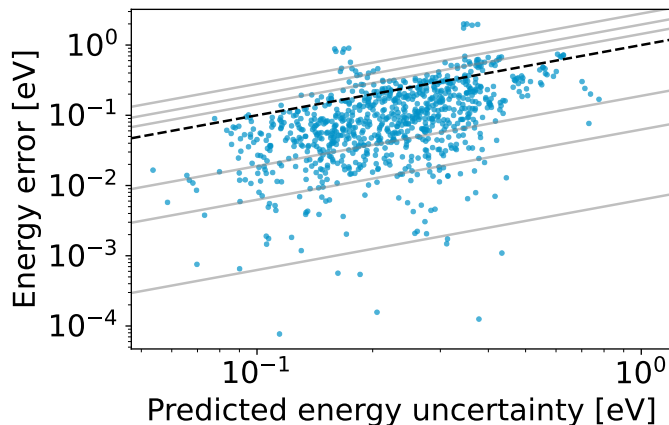
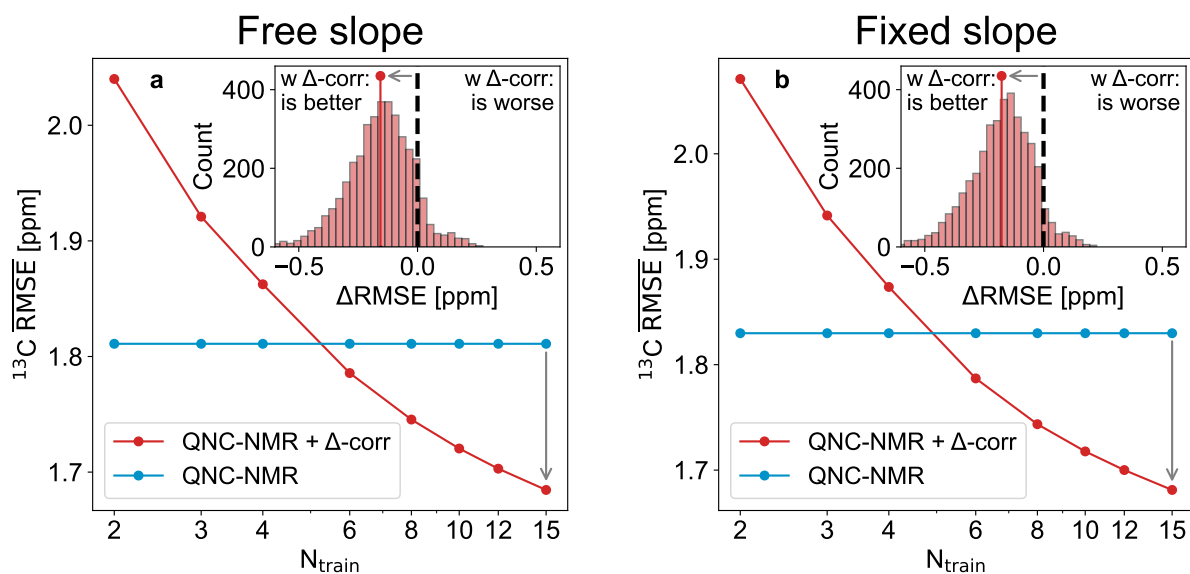


Figure S19: PET-MOLS predicted logarithmic potential energy uncertainties against logarithmic prediction errors of PET-MOLS. The grey lines represent quantiles of the expected error distribution at each predicted uncertainty level and serve as a visual reference. For instance, globally across the test set predictions, well-calibrated uncertainty estimates should place 90% of samples between the two outermost lines, which correspond to the 95th and 5th quantiles of the log-folded normal distribution.

S8 Learning from experiments: Additional tests

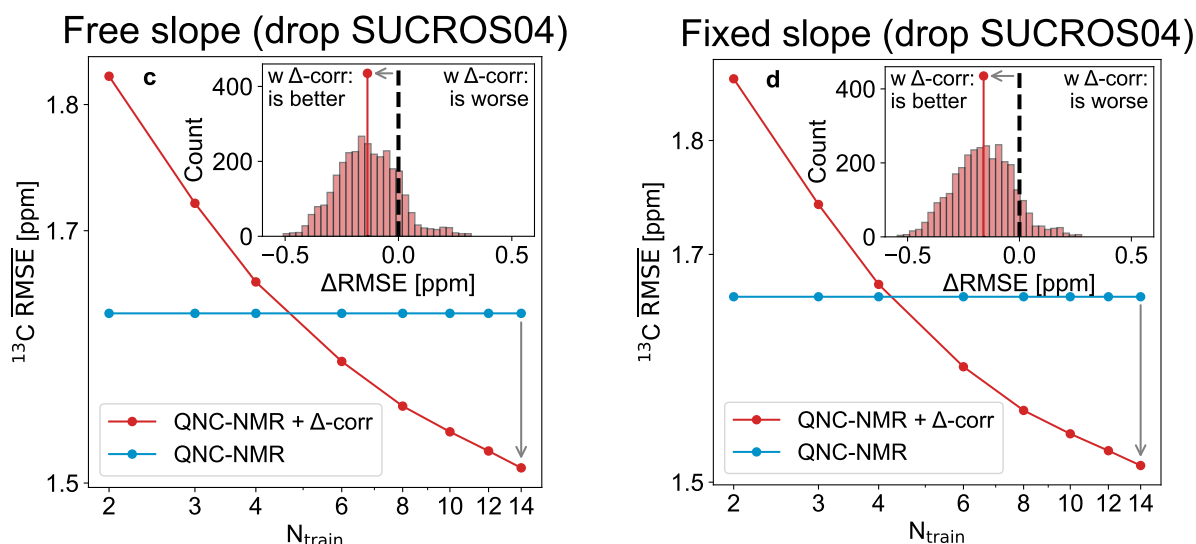
In this section we present additional experiments probing the stability of the training exercise correcting QNC-NMR with experimental data. In Fig. S20 we present learning curves applying the ELF framework to correct ^{13}C chemical shift predictions from experimental data. The experimental shifts are listed in Table S2, and are identical to those used for benchmarking the QNC-NMR protocol. Corrected last layer weights w_{corr} are determined by first converting QNC-NMR predicted shieldings to shifts, employing regression parameters tabulated in table S4. Following this, the difference between QNC-NMR predicted shifts and experimentally measured values are minimized using the ELF formalism. In figure S20, we show the improvement in chemical shift prediction when only a limited number of experimental shifts are included in the training. We also test the robustness of our findings to changing composition of the arguably very small training set. In order to test the robustness, we remove structure SUCROS04 from the pool of training structures, which contains the environment with the largest QNC-NMR

prediction errors against experimental measurements (deviating by 9.3 ppm). We find that the conclusion



(a) Learning curve free slope

(b) Learning curve fixed slope



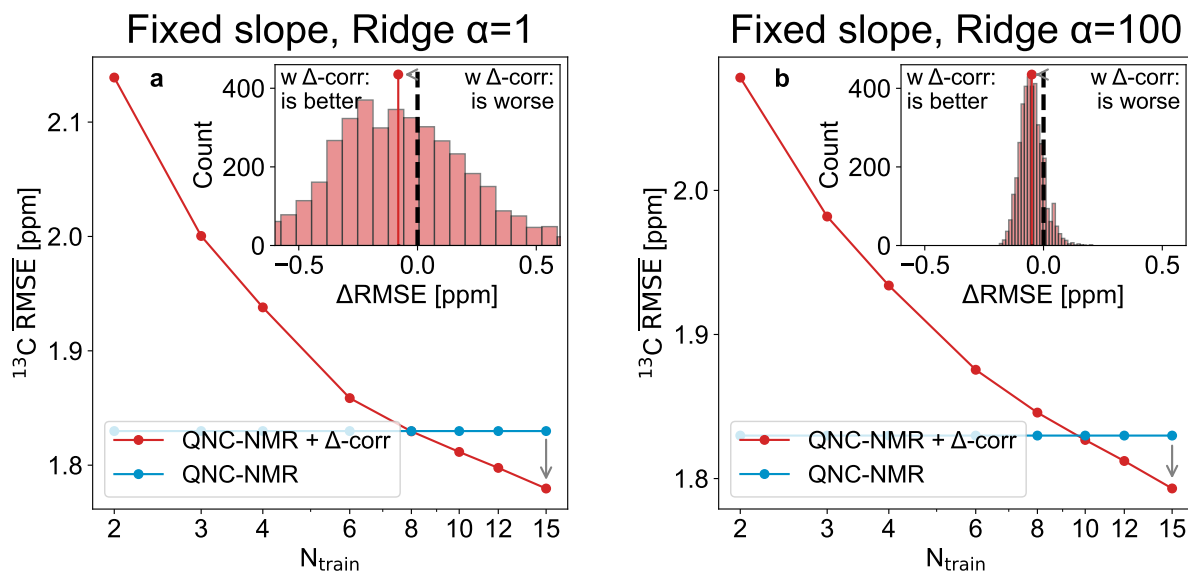
(c) Learning curve free sloped, after removing SUCROS04.

(d) Learning curve fixed sloped, after removing SUCROS04.

Figure S20: Learning curves of corrected QNC-NMR ^{13}C chemical shift predictions from experiments, probing the influence of fixed/free slope and removing SUCROS04 from the training and testing data. The inset shows a histogram of the change in prediction accuracy, ΔRMSE , between uncorrected and corrected predictions, computed over all $\binom{19}{4}$ splits of the 19 benchmark structures (or $\binom{18}{4}$ when SUCROS04 is removed) with a fixed test-set size of four structures. Splits to the left of the dashed line correspond to cases where the experimentally corrected QNC-NMR shielding predictions are more accurate on the test set, whereas splits to the right indicate cases where the correction reduces the prediction accuracy.

We also test the effect of varying the regularization strength (α) of the ridge regressor employed to find corrected weights. In Figure S21 we assess the effect of employing varying regularizer strengths in the finetuning from experiment for α value of 1 and 100. We find that

the overall trend persists that eventually after adding more structures experimentally finetuned QNC-NMR shift predictions become more accurate than uncorrected QNC-NMR predictions.



(a) Learning curve, employing a ridge regressor with regularization strength $\alpha = 1$.

(b) Learning curve, employing a ridge regressor with regularization strength $\alpha = 100$

Figure S21: Learning curves of corrected QNC-NMR ^{13}C chemical shift predictions from experiments, probing the effect of the regularizer strength. The inset shows a histogram of the change in prediction accuracy, ΔRMSE , between uncorrected and corrected predictions, computed over all $\binom{19}{4}$ splits of the 19 benchmark structures with a fixed test-set size of four structures. Splits to the left of the dashed line correspond to cases where the experimentally corrected QNC-NMR shielding predictions are more accurate on the test set, whereas splits to the right indicate cases where the correction reduces the prediction accuracy.

Supplementary References

1. Cordova, M. *et al.* A Machine Learning Model of Chemical Shifts for Chemically and Structurally Diverse Molecular Solids. en. *The Journal of Physical Chemistry C* **126**, 16710–16720 (2022).
2. Ramos, S. A., Mueller, L. J. & Beran, G. J. O. The Interplay of Density Functional Selection and Crystal Structure for Accurate NMR Chemical Shift Predictions. *Faraday Discussions* **255**, 119–142 (2024).
3. Kellner, M. *et al.* A Deep Learning Model for Chemical Shieldings in Molecular Organic Solids Including Anisotropy. *The Journal of Physical Chemistry Letters* **16**, 8714–8722 (2025).
4. Pozdnyakov, S. & Ceriotti, M. *Smooth, Exact Rotational Symmetrization for Deep Learning on Point Clouds in Advances in Neural Information Processing Systems* **36** (2023), 79469–79501.
5. Mazitov, A. *et al.* PET-MAD as a Lightweight Universal Interatomic Potential for Advanced Materials Modeling. *Nature Communications* **16**, 10653 (2025).
6. Veit, M. *et al.* Equation of State of Fluid Methane from First Principles with Machine Learning Potentials. *Journal of Chemical Theory and Computation* **15**, 2574–2586 (2019).
7. Pereyaslavets, L. *et al.* On the Importance of Accounting for Nuclear Quantum Effects in Ab Initio Calibrated Force Fields in Biological Simulations. *Proceedings of the National Academy of Sciences* **115**, 8878–8882 (2018).
8. Ceriotti, M. & Manolopoulos, D. E. Efficient First-Principles Calculation of the Quantum Kinetic Energy and Momentum Distribution of Nuclei. *Physical Review Letters* **109**, 100604 (2012).
9. Ceriotti, M., Bussi, G. & Parrinello, M. Nuclear Quantum Effects in Solids Using a Colored-Noise Thermostat. *Physical Review Letters* **103**, 030603 (2009).
10. Goodwin, R. D. & Prydz, R. Densities of compressed liquid methane, and the equation of state. *Journal of Research of the National Bureau of Standards. Section A, Physics and Chemistry* **76**, 81 (1972).
11. Jeffrey, G., Ruble, J. R., McMullan, R. & Pople, J. A. The crystal structure of deuterated benzene. *Proceedings of the Royal Society of London. A. Mathematical and Physical Sciences* **414**, 47–57 (1987).
12. Ehlert, S. *et al.* r2SCAN-D4: Dispersion Corrected Meta-Generalized Gradient Approximation for General Chemical Applications. *The Journal of Chemical Physics* **154**, 061101 (2021).
13. Zen, A. *et al.* Fast and Accurate Quantum Monte Carlo for Molecular Crystals. *Proceedings of the National Academy of Sciences* **115**, 1724–1729 (2018).
14. Zhai, Y., Caruso, A., Bore, S. L., Luo, Z. & Paesani, F. A “Short Blanket” Dilemma for a State-of-the-Art Neural Network Potential for Water: Reproducing Experimental Properties or the Physics of the Underlying Many-Body Interactions? *The Journal of Chemical Physics* **158**, 084111 (2023).
15. Reddy, S. K. *et al.* On the Accuracy of the MB-pol Many-Body Potential for Water: Interaction Energies, Vibrational Frequencies, and Classical Thermodynamic and Dynamical Properties from Clusters to Liquid Water and Ice. *The Journal of Chemical Physics* **145**, 194504 (2016).
16. Montero de Hijos, P., Dellago, C., Jinnouchi, R. & Kresse, G. Density Isobar of Water and Melting Temperature of Ice: Assessing Common Density Functionals. *The Journal of Chemical Physics* **161**, 131102 (2024).

17. Paesani, F., Zhang, W., Case, D. A., Cheatham, T. E. & Voth, G. A. An Accurate and Simple Quantum Model for Liquid Water. *The Journal of Chemical Physics* **125**, 184507 (2006).
18. Habershon, S., Markland, T. E. & Manolopoulos, D. E. Competing Quantum Effects in the Dynamics of a Flexible Water Model. *The Journal of Chemical Physics* **131**, 024501 (2009).
19. Cheng, B., Engel, E. A., Behler, J., Dellago, C. & Ceriotti, M. Ab Initio Thermodynamics of Liquid and Solid Water. *Proceedings of the National Academy of Sciences* **116**, 1110–1115 (2019).
20. Soper, A. K. The Radial Distribution Functions of Water and Ice from 220 to 673 K and at Pressures up to 400 MPa. *Chemical Physics* **258**, 121–137 (2000).
21. Štoček, J. R., Socha, O., Císařová, I., Slanina, T. & Dračinský, M. Importance of Nuclear Quantum Effects for Molecular Cocrystals with Short Hydrogen Bonds. *Journal of the American Chemical Society* (2022).
22. Engel, E. A., Kapil, V. & Ceriotti, M. Importance of Nuclear Quantum Effects for NMR Crystallography. *The Journal of Physical Chemistry Letters* **12**, 7701–7707 (2021).
23. Hu, E. J. *et al.* *LoRA: Low-Rank Adaptation of Large Language Models* 2021. arXiv: 2106.09685 [cs].
24. Bigi, F., Chong, S., Ceriotti, M. & Grasselli, F. A Prediction Rigidity Formalism for Low-Cost Uncertainties in Trained Neural Networks. *Machine Learning: Science and Technology* **5**, 045018 (2024).
25. Kellner, M. & Ceriotti, M. Uncertainty Quantification by Direct Propagation of Shallow Ensembles. *Machine Learning: Science and Technology* **5**, 035006 (2024).